

Use Authorization

In presenting this thesis in partial fulfillment of the requirements for an advanced degree at Idaho State University, I agree that the Library shall make it freely available for inspection. I further state that permission for extensive copying of my thesis for scholarly purposes may be granted by the Dean of the Graduate School, Dean of my academic division, or by the University Librarian. It is understood that any copying or publication of this thesis for financial gain shall not be allowed without my written permission.

Signature: _____

Date: _____

Habitability Potential of Enceladus:

An Analog Study of the Lō‘ihi

Seamount System in Hawai‘i

by

Angela H. Garcia

A thesis

submitted in partial fulfillment

of the requirements for the degree of

Master of Science in the Department of Geoscience

Idaho State University

December 2019

Copyright (2019) Angela H. Garcia

Committee Approval

To the Graduate Faculty:

The members of the committee appointed to examine the thesis of Angela H. Garcia find it satisfactory and recommend that it be accepted.

Shannon Kobs Nawotniak,
Major Advisor

Michael McCurry,
Committee Member

John V. Dudgeon,
Graduate Faculty Representative

Acknowledgements

I grew up on the beautiful Hawaiian island of Oahu. My curious eyes took in the mountains, the oceans, the stars—yearning to understand the mysteries surrounding my isolated paradise. Little did I know I would one day help direct a NASA underwater exploration mission off the coast of my childhood home from across the country in Rhode Island with Idaho State University making it all possible. It means the world to me that I have had the opportunity to grow as a scientist by learning from a place so close to my heart.

I have a lot of people and organizations to thank for the amazing opportunity. First, funding for the Systematic Underwater Biogeochemical Exploration Analog (SUBSEA) project was provided by NASA's Planetary Science and Technology Analog Research (PSTAR) program (award number 80NSSC17M0073), infrastructure by the National Oceanographic and Atmospheric Administration (NOAA) office of Ocean Exploration and Research (OER), and support by the Ocean Exploration Trust (OET). Special thanks to David Clague and team for sharing the Lō'ihī summit region 5m/pixel resolution map and Eric Christenson for collecting X-ray fluorescence geochemical data.

I would also like to thank my advisor Shannon Kobs Nawotniak and committee members John Dudgeon and Mike McCurry for training and feedback. Special thanks to SUBSEA team members Darlene, Ashley, Tamar, Dave, Khaled, Matthew, Zara, Vincent, Chris, Julie, Tim, and Ethan. To my past mentors Elisabeth Hausrath, Zoe Harrold, and Brad Sutter, I wouldn't be the scientist I am today without lessons I learned from you all while I was an undergraduate. I would like to thank Amber Hobbs, John Plisga, Meriwether Louis, and Michael Kassela for friendship, love, and support. Finally, Hawai'i is home to my amazing supportive parents, Akeyo and Wayne and my fierce older sisters, Nadia and Mandy; I love you all and hope to see you again very soon.

Table of Contents

List of Figures	vii
List of Tables	xi
Abstract	xii
Chapter 1. Introduction/Background	1
1.1 Context and Organization	1
1.2 Microbial Habitability Potential	3
1.3 Characterization of Enceladus	5
1.4 Lō‘ihi Seamount Field Site Description	7
1.5 Hydrothermally-Influenced Submarine Mafic Rock Alteration	11
Chapter 2. Methods	13
2.1 Sample Collection	13
2.2 Sample Processing/Analysis	15
Chapter 3. Results	18
3.1 Thin Section Results	18
3.1.1 Pohaku	19
3.1.2 Loihau	22
3.1.3 Spillway	23
3.1.4 Tower	24
3.2 Major and Minor Element Oxide Results	32

3.3 Trace Element Results	36
Chapter 4. Discussion	42
Chapter 5. Conclusion.....	46
Chapter 6. Closing Statement	48
References.....	49

List of Figures

Figure 1. NASA/JPL-Caltech conceptual illustrations of the interior of Enceladus. These illustrations are based on results from the Cassini spacecraft when it analyzed particles ejected from the South Polar Region. Note the mafic rocky core with overlying salt-water ocean. These illustrations are not to scale.5

Figure 2. Lō‘ihi seamount summit region and exploration area of the 2018 SUBSEA scientific cruise (NA100). The color of the markers indicate the lava type (purple indicates alkalic, red indicates tholeiitic, and green indicates transition between alkalic and tholeiitic). The shape of the marker indicates when the rock was collected. Bathymetry is 5m/pixel obtained from Clague et al. (2019).9

Figure 3. Basalt samples collected proximal to hydrothermal vent orifices. The dashed white circle is the location of the vent orifice and the white arrow points to the sample collected. The sample collected for M34 was collected ~15m above the vent orifice. The green lasers above the vent orifice on M2 and M34 are 10cm apart (white rectangle).14

Figure 4. Example micrographs of olivine phenocrysts within categories 1-3 based on degradation from alteration. The top left pair of micrographs are olivine in category 1, optically unaltered (Sample ID: NA100-84Ext). The top right pair of micrographs are olivine in category 2, partially altered (Sample ID: NA100-37Ext). Partial alteration of olivine was often paired with amorphous silica outlining the rim and pale yellow spherical carbonates within altered olivine grain boundary. The bottom four micrographs are olivine in category 3, completely altered olivine phenocrysts. The bottom left pair of micrographs have complete pseudomorphological replacement of olivine with phyllosilicates and silica (Sample ID: NA100-30). The bottom right pair of micrographs have

complete replacement of olivine with void space and partial secondary infill by carbonates (Sample ID: NA100-37Ext). PP: plane polarized light; XP: crossed polarized light.....16

Figure 5. Petrographic micrographs of carbonates siderite (core) and siderite-magnesite (rim) within vesicles in thin sections of basalts collect from Lō‘ihi hydrothermal vents (Spillway; NA100-37-E). PP: plane polarized light. XP: crossed polarized light.....20

Figure 6. Petrographic micrographs with corresponding SEM/EDS major element maps (Si, O, Fe, Mg, Ca) of siderite (core) and siderite-magnesite (rim) within basalt vesicles of Spillway thin section (NA100-37I). PP: plane polarized light. XP: crossed polarized light.....21

Figure 7. Petrographic micrographs with corresponding SEM/EDS major element maps (Si, O, Fe, Mg, Ca) of Fe-oxide precipitates, likely hydrothermal iron oxide deposit, associated with fresh glass of basalt of Loi hau (NA100-75E). Se: secondary electron detector. PP: plane polarized light. XP: crossed polarized light..... 22

Figure 8. Petrographic micrographs with corresponding SEM/EDS major element maps (Si, O, Fe, Mg, Ca) of splotchy red and grey groundmass corresponding to specific element enrichments as well as pyrite fracture infill Tower thin section (NA100-30). Se: secondary electron detector. PP: plane polarized light. XP: crossed polarized light.....25

Figure 9. Billet cross section displaying the light colored exterior with dominantly white vesicle infill and dark interior with dominantly red-orange infill. This section also displays a ~mm thick pyrite rind on the exterior (NA100-31).....26

Figure 10. a) Chemically-pure precipitated quartz within a vesicle in Tower thin section (NA100-31). b) chemically-impure precipitated quartz within a vesicle in Tower thin section (NA100-31).....27

Figure 11. The petrographic micrographs and corresponding SEM/EDS elemental maps illustrate the ~mm thick pyrite encrustation on the Tower thin section (NA100-31).....28

Figure 12. The petrographic micrographs and corresponding SEM/EDS elemental maps illustrate pyrite pseudomorphological replacement of euhedral olivine in the Tower region (NA100-30).. 29

Figure 13. The petrographic micrographs and corresponding SEM/EDS elemental maps illustrate bladed pyrite within vesicle and red-orange siderite-magnesite rimming vesicle within the Tower region (NA100-30).....29

Figure 14. The petrographic micrographs illustrating <10um spheres of jarosite within a vesicle directly associated with amorphous impure quartz, quartz, and pyrite globules within the Tower region (NA100-31).....30

Figure 15. The top two micrographs do not correspond to the SEM/EDX maps. The petrographic micrographs illustrate the Ti-Ba-V-O blades at Tower thin section (NA100-31). The SEM/EDX image contains these blades interbedded with pyrite and minor silica.....31

Figure 16. a) Talc to Pyrophyllite pseudomorphologically replacing olivine b) rim is Na-Al silicate within a vesicle with Mg-Fe-Al silicate in the interior c) Mg-Fe-Al silicate pseudomorphologically replacing olivine phenocryst directly associated with minimally altered pyroxene.....32

Figure 17. TAS diagram plotting the basalts collected close to hydrothermal vents (Pohaku, Loi hau, Spillway, and Tower) and the basalts collected away from known hydrothermal activity. The exterior of the hydrothermally-altered basalts have a thick outline compared to the interior. Only the interior section of ambient-water interaction basalts are plotted in the TAS diagram due their similar values to the exterior..... 34

Figure 18. The element oxide exterior to interior difference in wt.%. The largest enrichments in the exterior are in Si, Al, and Ca and the largest depletions in the exterior is in Fe and Mg.....35

Figure 19. The trace element concentration (ppm) relative percent enrichment or depletion calculated using Equation 2. Rb, La, Sm, Pb, Th, and U were removed from this figure because of low ppm concentrations (<15ppm) causing the percent differences from exterior to interior to be exaggerated. F, S, Cl values are considered an approximation, with uncertainties of at least 10% as shown with the error bars.....39

List of Tables

Table 1. Locations of hydrothermal vent sampling sites.....	13
Table 2. Thin section modal abundances for basalt collected in close proximity to hydrothermal vents.....	18
Table 3a. Chemical composition of basalt samples collected in close proximity to hydrothermal vent orifices (wt.%) obtained by XRF analysis.....	33
Table 3b. Chemical composition of basalt samples collected in from the ambient group, away vent orifices (wt.%) obtained by XRF analysis.....	34
Table 4a. Chemical composition of basalt samples collected in close proximity to hydrothermal vent orifices (ppm) obtained by XRF analysis.....	37
Table 4b. Chemical composition of basalt samples collected in from the ambient group, away vent orifices (ppm)obtained by XRF analysis.....	38

Habitability Potential of Enceladus: An Analog Study of the Lō‘ihi Seamount System in Hawai‘i

Thesis Abstract—Idaho State University (2019)

Measurements from the *Cassini* orbiter revealed that Saturn’s moon, Enceladus contains a hydrothermally-active liquid water ocean underneath its icy shell. This thesis contributes to understanding the microbial habitability potential of Enceladus by evaluating the major controls on the chemical exchange between submarine rocks, hydrothermal fluids, and seawater at the Lō‘ihi seamount. Lō‘ihi is a compelling hydrothermal analog system for Enceladus due to its environmental conditions (temperature, pressure), host rock type (ultramafic/mafic silicate), and geologic setting (hotspot). We utilized petrographic and scanning electron microscopy paired with major and trace element spectrometry to quantify distinct chemical populations of minerals, make qualitative observations of mineral spatial distribution, and compare the relative bulk geochemical abundance of the exterior to interior within samples from across Lō‘ihi. These analyses indicate that Lō‘ihi has a spatially and temporally complex hydrothermal system with large changes in composition, and therefore potential habitability, over centimeter and larger scales.

Key Words: Habitability, Hydrothermal, Basalt, Alteration, Lō‘ihi Seamount, Enceladus, Analog

Chapter 1. Introduction/Background

1.1 Context and Organization

In the search for possible microbial life beyond Earth, NASA’s “follow the water” strategy focused attention on Ocean Worlds in our Solar System—one such world is Saturn’s moon, Enceladus. Enceladus is a high-priority future astrobiology target since it contains a hydrothermally-active liquid water ocean underneath its icy shell (Mckay et al., 2014). Before multi-billion-dollar missions can take place, we must first address fundamental knowledge gaps about volcanically-hosted submarine hydrothermal systems, including to what extent hydrothermal fluids at the seafloor influence seawater-dominated mafic rock alteration processes and, subsequently, which elements are readily available for microbes to use as nutrient and energy sources and in what concentrations and spatial distributions they exist. We hypothesize that mineralogical and chemical changes of the host rock basalt at hydrothermal vent sites are fundamentally different than typical seawater alteration and that these changes improve microbial habitability potential. This thesis evaluates the effects of chemical exchange between submarine rocks, hydrothermal fluids, and seawater at the Lō‘ihi seamount analog environment, and hence which elements are present and in what distributions they are available for microbes to potentially use as energy and nutrient sources.

This thesis focuses on the results for the geologic branch within the NASA Systematic Underwater Biogeochemical Exploration and Analysis (SUBSEA) analog project for the Lō‘ihi site during the 2018 cruise. The geological results will be combined with fluid geochemical and microbiological results from research collaborators at other institutions within SUBSEA to more clearly define the Lō‘ihi hydrothermal system. The SUBSEA study is unique in that it combines

geology, chemistry, and microbiology from the same orifices at the same time and specifically collects water and microbes from within the vents instead of from the surrounding precipitate and microbial mats. SUBSEA is the first cruise to return to Lō‘ihi in over a decade, thus we provide an important time series point for long-term studies of the active and evolving system. Since previous geologic studies at the hydrothermal vent orifices focused on hydrothermal mound deposits and sediment, this project also makes an important contribution to understanding the hydrothermal alteration of the basalt in the system, and, thereby, begin to constrain the potential sources and limits of nutrients available from the rock.

This thesis is organized into 6 chapters: introduction/background, methods, results, discussion, conclusion, and closing statement. The introduction/background, Chapter 1, addresses concepts of microbial habitability, characterization of Enceladus’ environment, and geologic/geochemical setting of the Lō‘ihi seamount hydrothermal system. The methods, Chapter 2, describes the remotely operated vehicle (ROV) sample collection process and sample preparation, including microscopic (petrographic; scanning electron) and spectrographic (X-ray fluorescence; electron dispersive) analyses used on geologic thin sections and rock powders. The results, Chapter 3, reports the petrographic primary mineral modal abundances and secondary mineral assemblages of basalts collected at each hydrothermal vent site, and the major element oxide and trace element concentrations of the exterior to interior of each rock sample. The discussion (Chapter 4), describes the implications of the secondary mineral and bulk geochemistry results within Lō‘ihi’s hydrothermal system and relates this work to Enceladus. The conclusion (Chapter 5), summarizes the local and regional scale spatial and temporal complexity results at Lō‘ihi. Finally the closing statement (Chapter 6), puts the work completed in this thesis into context within the larger SUBSEA project goals.

1.2 Microbial Habitability Potential

Rocks at the seafloor provide substrate for elements and nutrients required for microbial life to concentrate and be released via fluid-rock interaction, as well as act a record of the surrounding aqueous history. In astrobiology/exobiology, microbial habitability is defined as the environmental condition's capability to support microbial life, whether or not the location under consideration is actually inhabited (e.g., Farmer, 2018), and is evaluated in terms of the environment's availability and temporal persistence of liquid water, energy, and nutrients. Through the lens of habitability, there are three outcomes possible for another planetary body: a uninhabitable environment that is uninhabited, a habitable environment that is uninhabited, or a habitable environment that is inhabited (e.g., Lineweaver and Chopra, 2012). Therefore, high habitability potential does not equate to an inhabited environment. This work aims only to better define the habitability potential (energy and nutrient sources and availabilities) and not to argue whether Enceladus is an inhabited environment.

In the search for possible microbial life beyond Earth, NASA has focused the search to planetary bodies that have sufficient evidence of liquid water. Liquid water is a priority because there is no alternative for life as we know it; liquid water facilitates biochemical reactions and nutrient transport. Enceladus has abundant geological, geophysical, and geochemical evidence (Section 1.3) supporting the existence a subsurface salt water ocean under a km-thick ice shell (Fig. 1). Once the requirement of liquid water is satisfied, the energy and nutrient budgets can be evaluated.

All organisms need an energy source. In photosynthesis, organisms use photons from the sun to synthesize energy. However, in a subsurface ocean, where light cannot penetrate, chemosynthetic organisms utilize chemical disequilibrium to synthesize energy. Chemosynthetic

energy is gained through redox coupling (i.e. oxidation—reduction). For example, mafic rocks contain reduced elements like Fe^{2+} that, when released via water-rock interactions, may be biotically oxidized to Fe^{3+} producing an energy source. Chemosynthetic organisms such as iron oxidizing bacteria and methanogens thrive at the Lō‘ihi seamount and may also be able to survive on similar environments beyond Earth that contain an appropriate chemical aqueous environment (i.e. Enceladus).

All organisms also need a sufficient nutrient source to metabolize. The basic elements of life are carbon, nitrogen, hydrogen, oxygen, phosphorus, and sulfur (CHNOPS). Therefore special attention is placed on the budgets of CHNOPS nutrients and elements with high energy yield (redox potential) such as iron and their availability within the aqueous environment (Burgin et al., 2011). Rock substrates provide concentrated sources for vital CHNOPS nutrients. Hence on local spatial scales the physical and chemical conditions of the aqueous environment such as temperature, pressure, acidity, and salinity place constraints on habitability. The hydrothermal alteration of mafic rocks like basalt releases both energy and nutrient sources that microorganisms may metabolize.

The motivation for this research is to better constrain the habitability conditions of Enceladus in terms of energy and nutrient budgets via studying water-rock interactions of a terrestrial analog environment, Lō‘ihi. Submarine basalts described herein were collected in close proximity to hydrothermal vent orifices and at distal locations across Lō‘ihi. At these same vent orifices, fluid and microbiology samples were collected and are being analyzed at our partner institutions Woods Hole Oceanographic Institute and Arizona State University. Therefore the combined datasets collected during the fieldwork at Lō‘ihi will contribute to the state of knowledge

about the microbial habitability potential of an expanded range of analog vent systems for Enceladus.

1.3 Characterization of Enceladus

Enceladus is 500 km in diameter, the sixth-largest moon of Saturn, and the brightest satellite in the Solar System. Its high-albedo consists of a reflectance spectrum dominated by pure water due to the coating of fine ice particles that also constitute Saturn's E-ring (e.g., Porco et al., 2006). There is geophysical, geological, and geochemical evidence from the *Cassini* spacecraft that indicate the presence of a global ocean of liquid water beneath a km-thick icy shell on Enceladus (Fig.1). *Cassini's* fly-by gravity density measurements revealed the moon has an ice shell, a liquid component, and a rocky core (e.g., Spencer et al., 2006; Iess et al., 2014); further reconnaissance found Enceladus to have an internal heat source (Spencer et al., 2006). Enceladus is only the third planetary body sufficiently geologically active for its internal heat to be detected

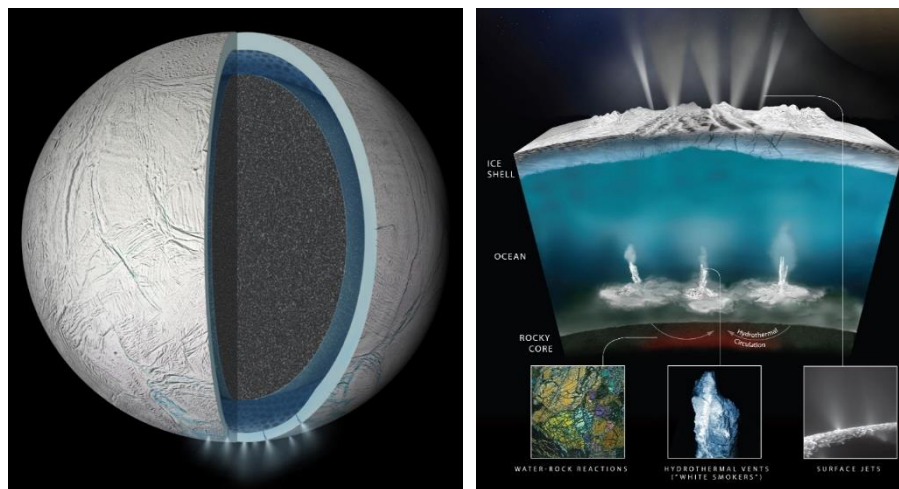


Figure 1. NASA/JPL-Caltech conceptual illustrations of the interior of Enceladus. These illustrations are based on results from the *Cassini* spacecraft when it analyzed particles ejected from the South Polar Region. Note the mafic rocky core with overlying salt-water ocean. These illustrations are not to scale.

remotely (Spencer et al., 2006). The core of Enceladus is assumed to be close to chondritic compositions (average concentration of non-volatile elements in the Solar System) if it did not undergo igneous differentiation by partial melting (e.g., Schubert et al., 2007; Sekine et al., 2015; Glein et al., 2018). If it did, it would likely be ultramafic to mafic rock compositions prior to alteration (Zolotov, 2007). Density measurements, *Cassini* observations, and numerical simulations support Enceladus to be a differentiated body with a metal-rocky core (e.g., Schubert et al., 2007).

Cassini also flew through the plume emanating from tectonic fractures at Enceladus' south pole and measured its geochemical constituents. A majority of what it detected was sodium-salt-rich ice particles, further supporting there is a salt water ocean beneath the km-thick icy shell (e.g., Zolotov, 2007; Postberg et al., 2009; Postberg et al., 2011, Spencer and Nimmo, 2013). *Cassini* also detected molecular hydrogen (H_2) (e.g., Seewald et al., 2017; Waite et al., 2017) and nano-sized silica (SiO_2) particles (e.g., Hsu et al., 2015; Sekine et al., 2015), which support the hypothesis that Enceladus contains unstable free chemistry within the liquid water reservoir due to active hydrothermal processes interacting with rocks (Postberg et al., 2009; Hsu et al., 2015; Sekine et al., 2015; Waite et al., 2017).

H_2 is readily produced via the hydrothermal alteration of reduced ultramafic and mafic rocks. For example, when reduced Fe-bearing minerals, such as olivine ($(Mg^{2+}, Fe^{2+})_2SiO_4$), interact with surrounding water (H_2O), the reduced iron acts as sink for the oxygen, releasing H_2 from H_2O (e.g., Waite et al., 2017). As H_2 is far from chemical equilibrium it does not last long in this system, hence the argument that Enceladus contains *ongoing* hydrothermal processes (e.g., Seewald et al., 2017). H_2 chemical disequilibria is frequently exploited by microbes in hydrothermal vents on Earth via methanogenesis. Methanogenesis is a chemosynthetic metabolic

pathway where microbes combine H_2 with CO_2 to produce CH_4 , or methane—all common chemical products in Earth magmatic hydrothermal systems (e.g., Lowenstern, 2001).

The detection of nano-sized SiO_2 particles also supports ongoing hydrothermal activity at Enceladus since the narrow particle size range is uniquely produced when SiO_2 saturation is reached upon cooling of slightly alkaline hydrothermal fluids (e.g., Sekine et al., 2015; Hsu et al., 2015). The most plausible source of SiO_2 would be from a rock-related system (Hsu et al., 2015). Laboratory experiments constrains the ranges of pH, temperature, salinity, and pressure this chemical product can form (Sekine et al., 2015; Hsu et al., 2015).

These lines of evidence combine to suggest that the seafloor of Enceladus is a porous rocky silicate, likely mafic to ultramafic in composition, interacting with heated alkaline water (~50-200°C) at pressures of 10-50MPa and pH values of ~8.5 (Sekine et al., 2015; Waite et al., 2017). This environment is astrobiologically relevant due to water-rock interactions releasing redox coupling energy sources and nutrients.

1.4 Lō‘ihi Seamount Field Site Description

Lō‘ihi is a Hawaiian underwater volcano rising ~3km from the floor of the Pacific Ocean to ~980 meters below sea level and is located 35km south of the Big Island (Fig. 2). Lō‘ihi is the youngest shield volcano in the Hawaiian-Emperor hotspot chain, with eruptions 400 kya through present day (Francis et al., 1993; Garcia et al., 1995). The summit of the Lō‘ihi volcano consists of three 300-370m deep pits: Pit of Death, East Pit, and Pele’s Pit. Pele’s Pit is youngest of the three and formed in 1996 during a large magmatic event (Duennebier et al., 1997; Caplan-Auerbach and Duennebier 2001a). Pele’s Pit and the surrounding area were the focus of the 2018 SUBSEA sampling campaign.

Lō‘ihi produces alkalic, tholeiitic, and transitional basalt compositions (e.g., Garcia et al., 1995). High alkali (K_2O+Na_2O) compositions reflect lower degrees of partial melting and suggest the beginning stages of volcanic growth (Garcia et al., 1995). As Lō‘ihi initially formed, the dominant rock type produced was alkali basalt. However, as Lō‘ihi has drifted closer to the Hawai‘i hotspot center and experienced higher temperatures and degrees of partial melting, it has erupted more tholeiitic basalt compositions (Garcia et al., 1995). Currently, tholeiitic basalt is the dominant rock type at Lō‘ihi, with minor alkali basalt components (e.g., Moore et al., 1982; Garcia et al., 1995; Guillou et al., 1997).

The known hydrothermal vents on the summit of Lō‘ihi are 1,100-1,325 m below the ocean surface and are surrounded by Fe-oxides (e.g., goethite) and Fe-clays (e.g., nontronite) and microbial mats. Geochemical reports from Lō‘ihi describe hydrothermal vent fluids to be typically $<100^\circ\text{C}$, $\sim 5.3\text{-}5.5$ pH, CO_2 -rich (up to $17\mu\text{M}$), Fe(II)-rich (up to $268\mu\text{M}$), and H_2S -poor (Karl et al., 1988; Emerson and Moyer, 2002; Garcia et al., 2006). Further fluid enrichments include elevated levels of dissolved Si, K, Li, Rb, Ca, Sr, Ba, Fe, Mn, and NH_4^+ relative to background seawater and depletions in SO_4^{2-} , O_2 , Mg, $87\text{Sr}/86\text{Sr}$, and NO_3^- (Karl et al., 1988; Sedwick et al., 1992; Wheat et al., 2000).

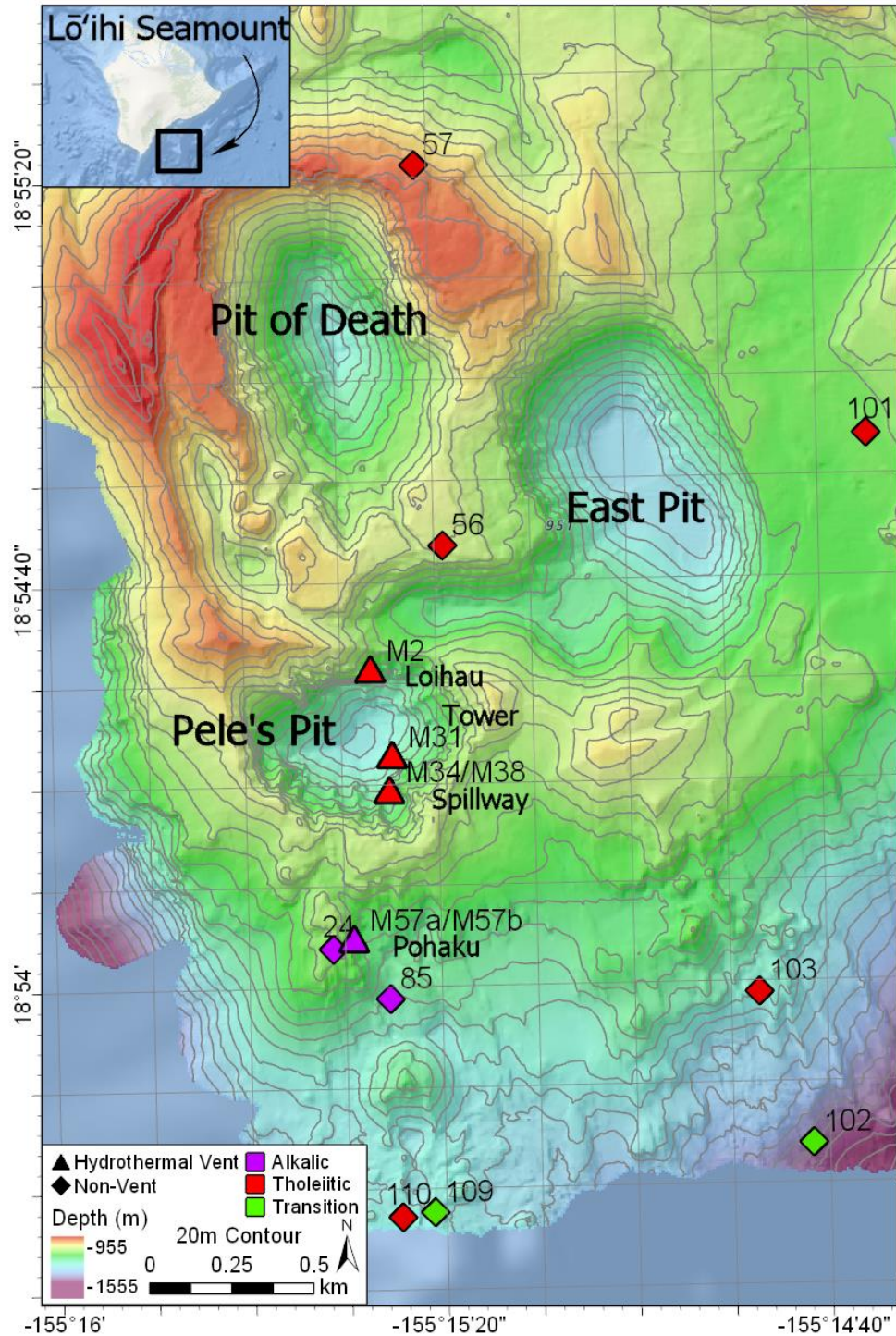


Figure 2. Lō'ihī seamount summit region and exploration area of the 2018 SUBSEA scientific cruise (NA100). The color of the markers indicate the lava type (purple indicates alkalic, red indicates tholeiitic, and green indicates transition between alkalic and tholeiitic). The shape of the marker indicates when the rock was collected. Bathymetry is 5m/pixel obtained from Clague et al. (2019).

Submersibles found extensive low temperature (15-30°C) hydrothermal venting at Lō`ihi at Pele's Vents in the 1980s (Malahoff et al., 1982; Sakai et al., 1987). In July-August 1996 there was a large tectonic and eruptive event that collapsed Pele's Vents to form Pele's Pit (Hilton et al., 1998; Wheat et al., 2000). This event changed the surface expression of Lō`ihi's hydrothermal system in terms of increased temperature (~200°C, possibly >330°C) (Hilton et al., 1998; Wheat et al., 2000). It was also the first evidence of high temperature (>250°C) Fe and Zn sulfide assemblages (e.g., pyrrhotite, wurtzite). In 1999, multiple diffuse low-temp vent sites (<80°C) were reported (Wheat et al., 2000 and Malahoff et al., 2006). In 2006, Glazer and Rouxel (2009) conducted a time series study that revealed hydrothermal fluids from Pele's Pit vents and southern vents at Pohaku had decreased in temperature (<55°C). A decade later, in 2018, the SUBSEA team visited Pele's pit and found continued temperature decreases to 18-41°C and relatively unchanged chemistry (Milesi et al., *in progress*).

Lō`ihi is a relevant analog hydrothermal system to Enceladus because Lō`ihi's isolated volcanic setting (hotspot) and environmental conditions (pressure, temperature) coincide with those of Enceladus (e.g., Garcia et al., 2006; Malahoff et al., 2006; Glazer et al., 2009; Hsu et al., 2015). Lō`ihi has fluid temperatures <100°C and pressures of ~10-13MPa, while Enceladus is postulated to have ~50-200°C and 10-50MPa temperature and pressure (Sekine et al., 2015; Waite et al., 2017). Furthermore, the rocks at Lō`ihi are hotspot basalts (mafic) broadly consistent with what may be a primary composition of Enceladus' rocky seafloor. Unlike mid-ocean ridge hydrothermal vents that occur at Earth's plate tectonic boundaries, Lō`ihi is part of an isolated volcanic system that exists in the middle of the Pacific Plate (intraplate). This intraplate or hotspot style of volcanism is common in the Solar System; plate tectonics, however, has only been unequivocally identified on Earth. Since isolated submarine volcanoes are postulated for

Enceladus (Baker et al., 1996; Baker et al., 2004) an intraplate hydrothermal system is preferred over a mid-ocean ridge hydrothermal system as an analog location to study the water-rock interactions that occur on the seafloor of Enceladus.

The rock composition and temperature range proposed for Enceladus are analogous to Earth's Lō'ihī seamount hydrothermal vent field, which is host to abundant chemosynthetic life. On Earth, hydrothermal activity and water-rock chemical exchanges at the seafloor create conditions favorable to microbes (e.g., Thorseth et al., 1995). These conditions liberate chemical reductants that, when combined with oxidants in the overlying ocean, provide redox couples favorable for microbial metabolisms (Amend et al., 2011). For example, on Lō'ihī, a majority of the local bacteria consortia (microbial mats) are supported by the Fe(II) to Fe(III) oxidation pathway or by the production of methane from hydrogen and water (e.g., Emerson and Moyer, 2002; Glazer and Rouxel, 2009; Hedrich et al., 2011; Escoube et al., 2015; Waite et al., 2017). The SUBSEA campaign used within-orifice sampling techniques to focus on organisms thriving within hydrothermal fluids before significant fluid-ocean mixing in the open ocean. For example, on Lō'ihī, a majority of the local bacteria consortia are supported by the Fe(II) to Fe(III) oxidation pathway or by the production of methane from hydrogen and water (e.g., Hedrich et al., 2001; Emerson and Moyer, 2002; Glazer and Rouxel, 2009; Waite et al., 2017).

1.5 Hydrothermally-Influenced Submarine Mafic Rock Alteration

Seawater and hydrothermal fluid interaction with basalt will break down the primary minerals and volcanic glass over time, then redistribute the elements as secondary mineral products or release the elements to seawater. Additional secondary products may form directly from magmatic vapor and fluids within the aqueous environment created by the mixing vent and sea fluids.

The fluids emanating from the vents at Lō‘ihi are the result of the various stages of mineral dissolution and precipitation and mixing of seawater. The cold seawater that saturates underlying basalt experiences high temperatures at depth. Hot water-rock interactions dissociate ions from host rock and saturate the fluid; these reactions produce reduced gases (e.g., CH₄, H₂, H₂S) that dissolve in fluid at the high pressure (e.g., Konn et al., 2015). Heated fluid has increased buoyancy, which initiates its rise back to the seafloor. The mixing of cold seawater and hot hydrothermal fluids at various stages beneath the ocean floor alters the equilibrium of solution—continuing the cycle of precipitation and dissolution.

Submarine basalts give rise to unique primary and secondary mineral alteration products (palagonite, goethite, nontronite, etc.) that over time create a geochemically broad spectrum of microbial habitats within the rock and nearby water. Water-rock interactions mobilize elements, allowing fluids and/or microbial metabolisms to remove and/or modify them. Basaltic glass is abundant at the seafloor and forms on all outer surfaces of submarine basalt, due to quenching in the cold water. Glass on the seafloor is thermodynamically unstable, which causes the basalt's glassy margins to break down rapidly relative to stony/crystalline interiors, and become easily accessible to the surrounding microbiome (Thorseth et al., 1995; Furnes et al., 2001; Stroncik and Schmincke 2001; Kruber et al., 2008). Thus, understanding the mineralogy, geochemistry, and texture of submarine basalt at our sampling locations are important to quantify alteration. We focused on understanding how alteration changes from the exterior to interior of samples because secondary products provide a geochemically broad spectrum of products and textural differences for microbes to utilize as energy and nutrient sources.

Chapter 2. Methods

2.1 Sample Collection

Submarine lava samples proximal and distal to hydrothermal vent orifices were collected by a remotely operated underwater vehicle (ROV) via robotic manipulator arm during the SUBSEA scientific cruise to the Lō‘ihi Seamount in August and September, 2018. The SUBSEA scientific cruise (NA100) was conducted from the *Exploration Vessel (E/V) Nautilus*, which is equipped with the ROV *Hercules* and ROV *Argus*. The SUBSEA team successfully conducted a systematic program of rock, vent fluid, and microbial sampling at five distinct hydrothermal vent sites (M2, M31, M34/M38, M57a, and M58b) previously identified during the Fe-Oxidizing Microbial Observatory (FEMO) scientific cruise in 2006 across the summit of Lō‘ihi (Glazer and Rouxel, 2009; Rouxel et al., 2018). These five vents fell within four regions at Lō‘ihi: Loihau (M2), Tower (M31), Spillway (M34/M38), and Pohaku (M57a and M57b) (Fig. 2 and Fig. 3) (Davis and Clague, 2003).

Table 1. Locations of hydrothermal vent sampling sites

	Pohaku M57a NA100-68	Pohaku M57b NA100-84	Loihau M2 NA100-75	Spillway M34 NA100-37	Tower M31 NA100-30,31,32
Latitude	18.901331°N	18.901387°N	18.908776°N	18.905578°N	18.906434°N
Longitude	155.258064°W	155.258086°W	155.257470°W	155.256927°W	155.256921°W
Depth (mbsl)	1186	1183	1180	1258	1299
Meters from vent ^a	<0	<0	<0	~15	<0
Vent Temp (°C) ^b	18	21	22	41	32
pH ^c	5.43-5.67	5.69-5.75	6.17-6.2	5.84-6.11	5.98-7.73

^a distance from vent orifice approximated from captured video. ^b temperature maximum recorded from the isobaric gas-tight (IGT) sampler of the hydrothermal fluid. ^c pH taken at 25C, bottom seawater had a pH of 7.39-7.83.

These hydrothermal vents were revisited to gain broad spatial distribution and representative temperatures within and outside Pele's Pit as well as continue the time-series assessment of the fluids at Lō'īhi. Additionally, hydrothermal vent sampling locations needed to meet minimum fluid flow requirements to be sampled by biology and geochemistry teams. The basalt samples were collected as close to vent orifices and fluid flow as possible, and were ideally at least 15cm diameter. The Suspended Particulate Rosette (SUPR) and Isobaric Gas-Tight (IGT) samplers were used to collect fluid from within the vent prior to release into the ambient seawater, and are being used by the microbiology and geochemistry branches of SUBSEA, respectively.

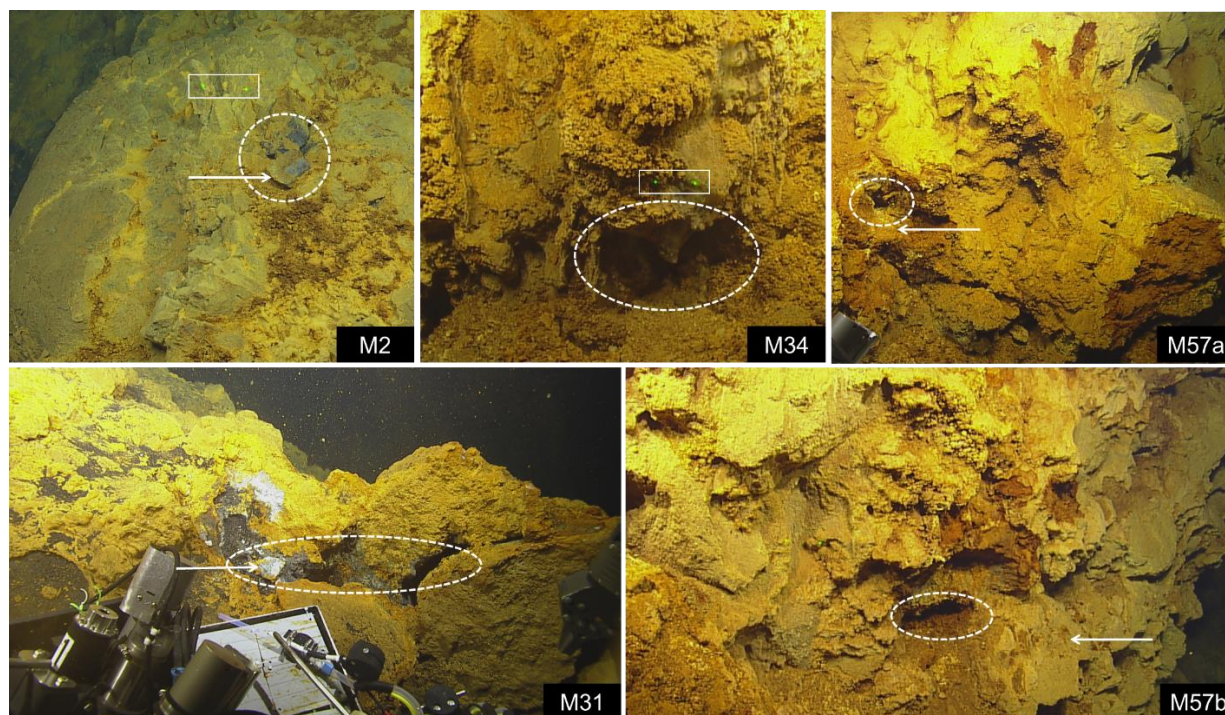


Figure 3. Basalt samples collected proximal to hydrothermal vent orifices. The dashed white circle is the location of the vent orifice and the white arrow points to the sample collected. The sample collected for M34 was collected ~15m above the vent orifice. The green lasers above the vent orifice on M2 and M34 are 10cm apart (white rectangle).

We analyzed the basalts altered at the hydrothermal vent orifices (Tower, Pohaku, Spillway, and Loihau regions) and basalts altered distally from any known hydrothermal vents

(ambient seawater altered basalt, n=9). The basalts collected for the ambient/background seawater group were spatially distributed across the summit of Lō‘ihi (Fig. 2). The ambient group’s seawater-altered basalt is used in this study to better constrain hydrothermal fluid influence on submarine basalt alteration; as such samples from both groups were processed using the same methodology.

2.2 Sample Processing/Analysis

We used microscopic and spectrographic analyses to measure the mineralogical and geochemical change over the outer few centimeters in basalt samples taken from hydrothermal vent areas and locations distant from all evidence of sustained thermal activity. We separated interior and exterior fractions of a given rock sample using a visible transition from relatively glassy to stony groundmass as seen in hand sample. The 1-1.5 cm glassy exterior of the rock was separated from the >2cm deep interior using a wet rock saw, with material from each portion used to create thin sections and powder for analyses. Thin sections were made by Wagner Petrographic.

The ambient group reflects chemical changes that occur during normal seawater conditions. The rate of palagonite formation (exterior glass hydration and alteration) for submarine lavas has been estimated at ~3um/1,000yr for young submarine lavas (Hekinian and Hoffert, 1975) and provided that the Lō‘ihi lavas are at most ~400,000 yr of age (Francis et al., 1993; Garcia et al., 1995), the scale of element exchange would still be at the mm-scale. However, challenges in processing fragile, small-volume samples at the mm-scale and the desire to compare directly with the more altered hydrothermal samples dictated that there was more value in using a thicker rind interpretation based on the glassy-stony transition.

The exterior and interior thin sections were evaluated for the modal composition of primary minerals, degree of olivine ((Mg²⁺, Fe²⁺)₂SiO₄) degradation, and broad identification of secondary

mineral assemblages and their spatial distributions. Petrographic point count techniques (1000 counts per slide) were used to estimate the modal composition of phenocrysts (plagioclase, pyroxene, olivine), groundmass, and vesicles (Table 2). The type of pyroxene was not differentiated in thin section. Olivine phenocrysts were categorized based on degradation from alteration; olivine alteration was used as a proxy for the total alteration because it is an expected constituent in all the basalt thin sections and is expected to be one of the first minerals to break down. The Fe to Mg content of olivine varies from the endmembers forsterite (Mg-rich) to fayalite (Fe-rich). The three categories of olivine alteration were based on optical properties (Fig. 4): category 1 were optically unaltered such that the phenocryst maintained expected optical properties and mineral shape relative to the groundmass; category 2 were partially altered, with remnants of the expected optical properties for olivine and the original mineral shape visible relative to the groundmass, but partially replaced by void space or secondary minerals; and category 3 were completely replaced by void space or pseudomorphological secondary mineral phases.

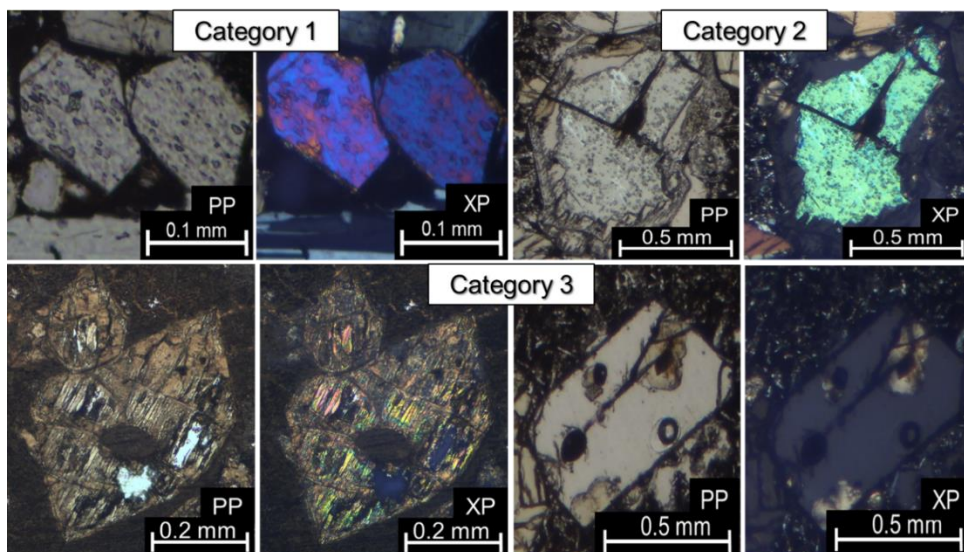


Figure 4. Example micrographs of olivine phenocrysts within categories 1-3 based on degradation from alteration. The top left pair of micrographs are olivine in category 1, optically unaltered (Sample ID:

NA100-84Ext). The top right pair of micrographs are olivine in category 2, partially altered (Sample ID: NA100-37Ext). Partial alteration of olivine was often paired with amorphous silica outlining the rim and pale yellow spherical carbonates within altered olivine grain boundary. The bottom four micrographs are olivine in category 3, completely altered olivine phenocrysts. The bottom left pair of micrographs have complete pseudomorphological replacement of olivine with phyllosilicates and silica (Sample ID: NA100-30). The bottom left pair of micrographs have complete replacement of olivine with void space and partial secondary infill by carbonates (Sample ID: NA100-37Ext). PP: plane polarized light; XP: crossed polarized light.

Secondary mineral assemblages were observed in thin section using petrographic optical properties and a field emission scanning electron microscope (SEM) connected to an energy dispersive spectrometer (EDS). The SEM (operating at 30kV) and EDS system was located at the Idaho State University (ISU) Center for Archaeology Materials and Applied Spectroscopy (CAMAS) under the advisement of Dr. John Dudgeon. Thin sections were carbon coated prior to SEM/EDS analysis to minimize the high electron charging from glass thin section. EDS enabled mapping of major element distributions as well as calculations of the total normalized atomic wt.% used to assist in mineral stoichiometry calculations. SEM/EDS was used to cross-check primary and secondary mineral identification, particularly for very small or morphologically unusual minerals, as well as to identify changes in the groundmass composition.

The exterior and the interior of the basalts were analyzed for bulk major (wt.%) and trace (ppm) elements by the Christiansen lab at Brigham Young University using wavelength dispersive X-ray fluorescence (XRF) operating at 50kV and 50mA. Powders were dried at 100°C for 10hrs and heated to 1000°C for 4hrs to measure loss on ignition (LOI). Prior to analysis, rock was coarsely crushed via sledgehammer and finely crushed by tungsten carbide ring and puck mill in a vibratory pulverizer.

Chapter 3. Results

3.1 Thin Section Results

The hydrothermal vent basalt thin section modal abundance results (1000 points/slide) are summarized in Table 2. The ambient seawater-altered basalts do not have point count results, but all olivine phenocrysts observed during thin section investigation fell within category 1. In addition there were no secondary mineral precipitates (e.g., carbonates, sulfides, silicates) observed in the ambient basalt group.

Table 2. Thin section modal abundances for basalt collected in close proximity to hydrothermal vents

	Pohaku-a ^a NA100-068 ^b				Pohaku-b ^a NA100-084 ^b				Loihau ^a NA100-075 ^b			
	Ext. ^c	$\pm err^d$	Int. ^c	$\pm err^d$	Ext. ^c	$\pm err^d$	Int. ^c	$\pm err^d$	Ext. ^c	$\pm err^d$	Int. ^c	$\pm err^d$
Vesicles (%)	33.3	1.5	18.4	1.2	40.0	1.5	26.0	1.4	1.2	0.3	2.7	0.5
Groundmass (%)	48.2	1.6	55.2	1.6	42.3	1.6	48.7	1.6	81.3	1.2	75.6	1.4
Plagioclase (%)	11.4	1.0	16.4	1.2	8.8	0.9	15.9	1.2	0.0	0.0	0.0	0.0
Olivine Cat. 1 (%)	1.4	0.4	4.2	0.6	2.9	0.5	3.6	0.6	16.3	1.2	20.2	1.3
Olivine Cat. 2 (%)	0.0	0.0	0.0	0.0	0.0	0.0	0.0	0.0	1.2	0.3	1.5	0.4
Olivine Cat. 3 (%)	0.0	0.0	0.0	0.0	0.0	0.0	0.0	0.0	0.0	0.0	0.0	0.0
Pyroxene (%)	5.7	0.7	5.8	0.7	6.0	0.8	5.8	0.7	0.0	0.0	0.0	0.0

	Tower ^a				Spillway ^a			
	NA100-030 ^b		NA100-032 ^b		NA100-031 ^b		NA100-037 ^b	
	Int. ^c	$\pm err^d$	Int. ^c	$\pm err^d$	Ext. ^c	$\pm err^d$	Int. ^c	$\pm err^d$
Vesicles (%)	0.5	0.2	2.0	0.4	10.5	1.0	13.6	1.1
Groundmass (%)	89.8	1.0	93.7	0.8	89.5	1.0	85.5	1.1
Plagioclase (%)	0.2	0.1	0.0	0.0	0.0	0.0	0.0	0.0
Olivine Cat. 1 (%)	0.0	0.0	0.0	0.0	0.0	0.0	0.0	0.0
Olivine Cat. 2 (%)	0.1	0.1	0.0	0.0	0.0	0.0	0.0	0.0
Olivine Cat. 3 (%)	4.9	0.7	4.2	0.6	0.0	0.0	0.0	0.0
Pyroxene (%)	4.5	0.7	0.1	0.1	0.0	0.0	0.9	0.3

^a Name of the area that contains the vent orifice. The spatial distribution can be viewed in Fig.2. ^b 2018 SUBSEA exploration cruise NA100 sample name. ^c Type of thin section, the outermost section named ‘Ext’ and innermost section named ‘Int’. ^d Reliability of point counts following Van Der Plas and Tobi (1965).

3.1.1 Pohaku

The Pohaku region is located ~350m south of Pele's Pit (Fig. 2). The basalt samples from the Pohaku area were collected from two vent orifices (Pohaku-a and Pohaku-b) in a cliff face at 1186mbsl and 1183mbsl, approximately 5m apart. The fluid emanating from Pohaku-a was 18°C with pH of 5.43-5.67, and Pohaku-b was 21°C with pH of 5.69-5.75.

Pohaku-a and Pohaku-b are the only alkalic lava types collected proximal to hydrothermal vent orifices during the SUBSEA cruise. Pohaku is the most phenocryst-rich vent site and is highly vesicular (up to 40% ± 1.5%) relative to the other vent sites. Pohaku is the only region in this study where there are more pyroxene than olivine and more plagioclase than pyroxene phenocrysts. The exteriors in both samples have higher vesicularity than the interiors. The high vesicularity is unusual for submarine lavas in general, but vesicularities of more than 50% have been reported at Lō'ihi (e.g. Moore et al., 1982). The seamount is under relatively great depth/pressure such that the high vesicularity is unusual (Fisher and Schmincke 1984; Schipper and White, 2010), however, the high vesicularity in this case is related to the high volatile content of Lō'ihi lavas (e.g., Byers et al., 1985; Garcia et al., 1993). The groundmass in Pohaku-a and Pohaku-b is composed of glass, minor secondary minerals, and microcrysts of plagioclase, pyroxene, olivine, and opaque oxides.

Pohaku-a and Pohaku-b represent the lowest degrees of olivine phenocryst alteration of all the vent areas, with 100% of the olivine phenocrysts in category 1 (Table 2). Pohaku is the only hydrothermal vent site studied where all olivine phenocrysts were unaltered.

One of the secondary minerals in the Pohaku region thin sections is a Mg, Fe, Ca-rich carbonate that infilled void spaces (Fig. 5, Fig. 6). The carbonate concretions were pale yellow to clear in plane light and had extremely high birefringence in crossed polarized light (Fig. 5). The carbonates were spherical or pentagonal in shape, with rim and core distinctions. The EDS point

spectra results support siderite (FeCO_3) with minor Mg and Ca substitution for Fe in cores and siderite-magnesite (FeCO_3 to MgCO_3) rims. These minerals were also observed in the Spillway and Loi hau thin sections. The carbonates found at Tower did not display the core-rim distinction but only had siderite throughout the globule.

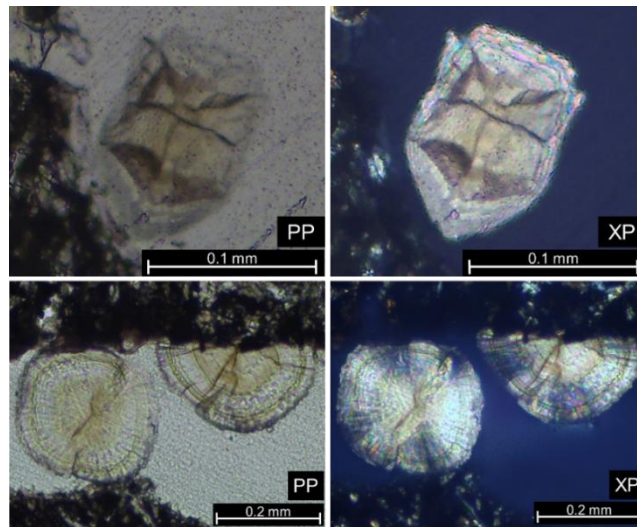


Figure 5. Petrographic micrographs of carbonates siderite (core) and siderite-magnesite (rim) within vesicles in thin sections of basalts collect from Lō'ihī hydrothermal vents (Spillway; NA100-37-E). PP: plane polarized light. XP: crossed polarized light.

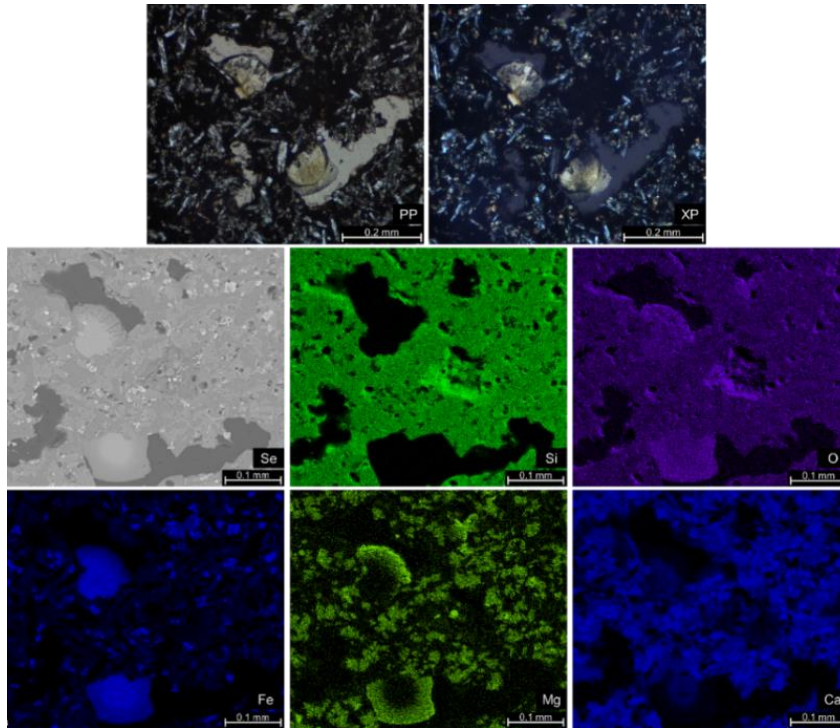


Figure 6. Petrographic micrographs with corresponding SEM/EDS major element maps (Si, O, Fe, Mg, Ca) of siderite (core) and siderite-magnesite (rim) within basalt vesicles of Spillway thin section (NA100-37I). Se: secondary electron detector. PP: plane polarized light. XP: crossed polarized light.

The only other secondary mineral identified in the Pohaku region thin sections was Fe-oxide (Fig. 7) associated exclusively with exterior glass. The Fe-rich globule aggregates were reddish-orange in plane light and went mostly extinct in crossed polarized light. These globules appear consistent with Fe-rich precipitate deposits of goethite ($\text{FeO}(\text{OH})$) and ferrihydrite ($\text{Fe}_{10}\text{O}_{14}(\text{OH})_2$) previously identified at Lō‘ihi (Toner et al., 2012).

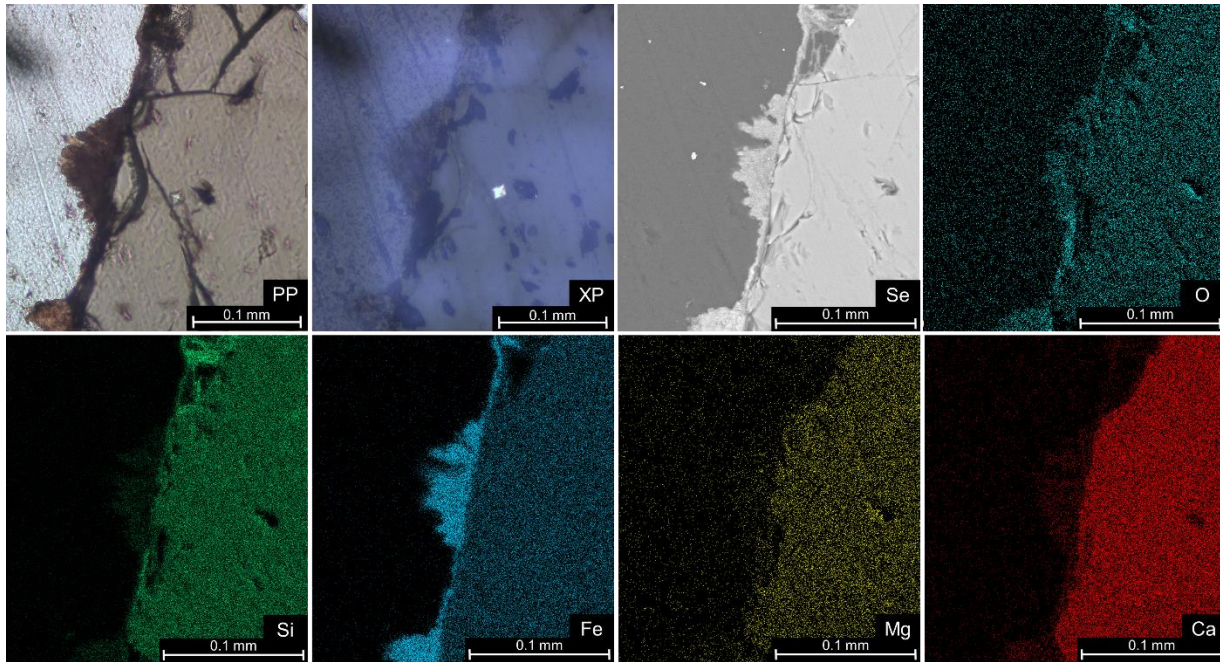


Figure 7. Petrographic micrographs with corresponding SEM/EDS major element maps (Si, O, Fe, Mg, Ca) of Fe-oxide precipitates, likely hydrothermal iron oxide deposit, associated with fresh glass of basalt of Loihau (NA100-75E). Se: secondary electron detector. PP: plane polarized light. XP: crossed polarized light.

3.1.2 Loihau

The Loihau vent area was a large pillow lava outcrop at 1180mbsl with hydrothermal fluid flowing through cracks in the basalt. The fluid emanating from the vent was 22°C with a pH of 6.17-6.2.

The Loihau lavas are tholeiitic, the most olivine-rich and pyroxene-poor, and have low vesicularity and no plagioclase phenocrysts (Table 2). The groundmass in Loihau is composed of glass, secondary minerals, and microcrysts of plagioclase, pyroxene, olivine, and opaque oxides.

The Loihau area has the second lowest degree of olivine phenocryst alteration with 93% in category 1 and 7% in category 2 for both the exterior and interior thin sections. Category 2 olivine

phenocrysts were partially altered to void space or secondary mineral infill by carbonates or amorphous quartz. There is no difference in degree or styles of olivine alteration from the exterior to interior of the basalt sample.

The secondary mineral assemblage at Loihau was the same as Pohaku (carbonates and Fe-oxides), but had the addition of amorphous quartz. The amorphous quartz was located within the boundary of altered olivine phenocryst fractures as infill. Amorphous quartz was clear in plane polarized light and went extinct in cross polarized light; EDS spectra suggested almost pure SiO₂ (see Fig. 4, category 2).

3.1.3 Spillway

The Spillway vent orifice was at the base of a cliff. Basalt collection directly at the vent orifice was not possible due to extensive hydrothermal precipitate covering the basalt such that the rock was not reachable via ROV. Therefore the basalt sample representing the Spillway area was collected ~15m directly above the orifice at 1258mbsl, as close to the path of fluid flow as possible. The fluid emanating at the orifice was 41°C with pH of 5.84-6.11 at the base.

Compared to the other vent sites, Spillway had fairly high vesicularity, low plagioclase, and moderate to high olivine content (Table 2). The Spillway area had the second highest degree of olivine phenocryst alteration, with a clear increase in alteration in the exterior relative to the interior of the samples: olivine phenocrysts in the exterior samples were ~20% unaltered, ~70% partially altered, and ~10% completely altered, while interior samples were ~86%, ~14%, and 0%, respectively.

Spillway had the same secondary mineral assemblage as Loihau: carbonates, Fe-oxides, and amorphous quartz, as well as the same spatial distribution of those minerals. An additional

point count, targeting secondary minerals, revealed Spillway had much more carbonate precipitate than Loihau (<1% for Loihau and ~8% for Spillway).

3.1.4 Tower

Multiple small basalt samples were collected from the same vent orifice in the Tower area instead of one large basalt sample; this was due to ROV accessibility and outcrop quality. The Tower vent was at 1299mbsl, and the fluid was measured at 32°C with pH of 5.98-7.73. Four samples were made into thin sections. In hand sample only one billet had clear exterior to interior distinction (NA100-31) with the exterior appearing visibly lighter in color than the interior (Fig. 9). In thin section however, that billet contained few to no phenocrysts and thus could not contribute to evaluating the degree of olivine phenocryst alteration. Fortunately two billets (NA100-30; NA100-32), which were colored similarly to the interior section of the billet previously described, contained olivine phenocrysts and thus were utilized in evaluating olivine phenocryst alteration.

The Tower region is the most olivine phenocryst poor, with low vesicularity, and large amounts of groundmass (Table 2). The groundmass in the Tower region (NA100-30; NA100-32) was distinct from the other vent sites in that a) it did not have clearly identifiable microphenocrysts and b) there were splotchy grey and red patterns visible in hand sample and thin section. The ruddy groundmass was enriched in Mg, K, and Fe, while the grey groundmass was enriched in Si, Na, Al (Fig. 8).

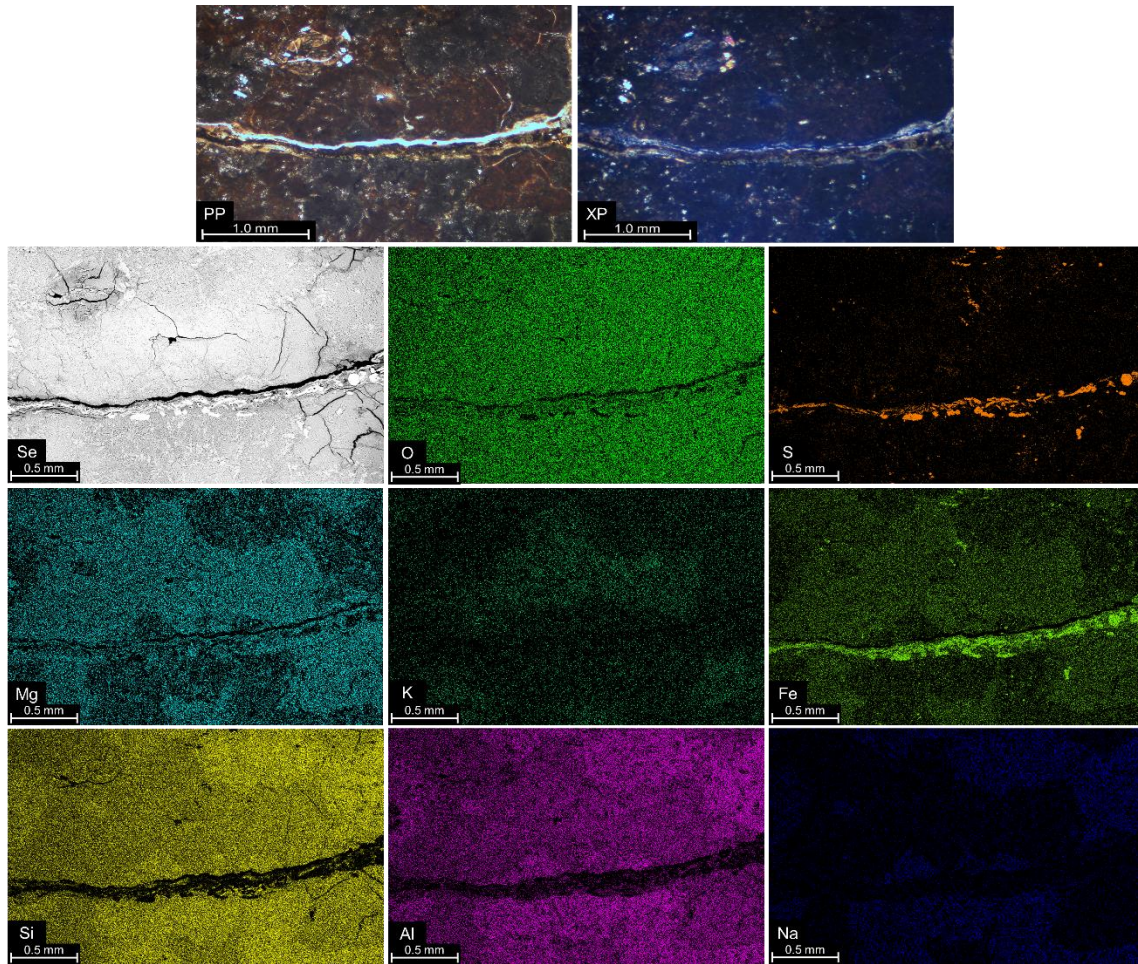


Figure 8. Petrographic micrographs with corresponding SEM/EDS major element maps (Si, O, Fe, Mg, Ca) of splotchy red and grey groundmass corresponding to specific element enrichments as well as pyrite fracture infill Tower thin section (NA100-30). Se: secondary electron detector. PP: plane polarized light. XP: crossed polarized light.

The Tower region had the highest degree of olivine phenocryst alteration, with 98% to 100% of the olivine phenocrysts completely altered, depending on the thin section (Table 2). Slightly altered pyroxene phenocrysts, the only ones observed in this study, co-occurred with completely altered olivine.

Tower region secondary minerals included quartz and siderite but these minerals presented different morphologies than in the Loihau and Spillway assemblages; Tower also had the addition

of sulfide/sulfates (pyrite; jarosite), complex silicates (talc-pyrophyllite, Na-Al silicate, Mg-Fe-Al silicate), and an unidentified Ba-Ti-V-O rich mineral. Unlike at the other vent locations, the vesicles in the Tower samples were mostly to entirely filled by secondary sulfide/sulfate, silicate, and carbonate deposits, leaving little void space in the rock; in contrast, Loi hau, Spillway, and Pohaku basalts maintained abundant void space.

In hand sample, the billet that had distinguishable exterior and interior sections (NA100-31) also had clear vesicle infill color distinction in hand-sample (Fig. 9). The exterior section had dominantly white infill, while the interior section infill was mostly red/orange. This distinction was not maintained through thin section processing, likely due to the fragile nature of the precipitates, and therefore was not explicitly clear during petrographic observations. However, the main white precipitates identified in thin section were quartz, and the dominant red/orange precipitates were siderite. This was the only sample from all vent sites where there was a distinct exterior or interior secondary mineral deposition location preference observed.



Figure 9. Billet cross section displaying the light colored exterior with dominantly white vesicle infill and dark interior with dominantly red-orange infill. This section also displays a ~mm thick pyrite rind on the exterior (NA100-31).

The quartz at the Tower region ranged from chemically pure, white, rounded masses and inclusions to tan amorphous/fibrous morphologies with Al, S, Cl, and Fe impurities totaling up to ~3% total normalized atomic wt.% (Fig. 10a). The chemically pure quartz was present in vesicles

and within completely altered olivine. The chemically impure amorphous quartz was only identified rimming vesicles (Fig. 10b). The spatial distribution of quartz differs in Tower from Loihau and Spillway. At Tower, quartz dominantly precipitated in vesicles in the exterior, whereas at Loihau and Spillway amorphous quartz was exclusively identified infilling altered phenocrysts in the exterior and interior sections. This change in Si deposition behavior appears to be a reflection of the source of Si during the time of deposition. Where in Tower there was abundant Si percolating through the basalt in fluids enabling deposition in vesicles, in Loihau and Spillway the Si was likely more closely sourced from the proximal altered olivine.

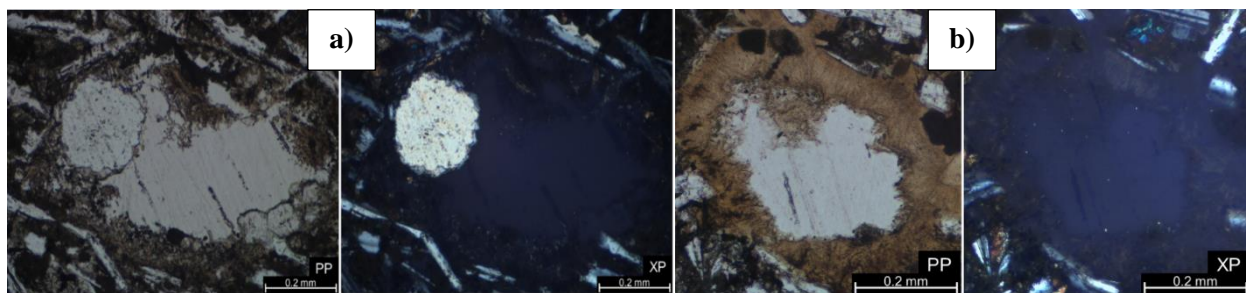


Figure 10. a) Chemically-pure precipitated quartz within a vesicle in Tower thin section (NA100-31). b) chemically-impure precipitated quartz within a vesicle in Tower thin section (NA100-31).

The carbonates within the Tower area were siderite-magnesite, which was also identified in Loihau, Spillway, and Pohaku. However, instead of pale to dark yellow (in PP), the siderite-magnesite at Tower ranged from red-orange to pale yellow. The siderite-magnesite also was not rimmed by additional carbonates such as in Loihau, Spillway, and Pohaku. The morphology was also different in the Tower samples, with the siderite-magnesite forming aggregates of spheroids (~10 μ m) that occasionally merged into a smooth massive infill, while at the other vent sites the spheroids were individual and ~10x larger.

The dominant sulfide identified in Tower was pyrite (FeS₂), which was visible in hand sample, with multiple morphologies seen in the thin sections. EDS consistently confirmed that the mineral was pyrite and that the morphological changes were not actually the result of local

transitions to chalcopyrite or other minerals. Several, but not all, samples had ~mm thick encrustation of botryoidal pyrite surrounding the exterior of the sample (Fig. 11). Pyrite pseudomorphologically replaced olivine phenocrysts (Fig. 12) and deposited as blades and cubes within fractures and in the interiors of vesicles (Fig. 8; Fig. 13). Pyrite assemblages in sediments and hydrothermal mounds were previously reported at Lō'ihī's north vents (Loihau) and north east vents (did not visit) (David and Clague 1998; Davis et al., 2003). High-temperature mineral assemblages (pyrite, marcasite, pyrrhotite, wurtzite, and barite) had never been identified at Lō'ihī prior to the work of David and Clague (1998) at the northern vent sites (Loihau); we now can also confirm the presence of high-temperature mineral assemblages (pyrite; jarosite) at the south east vents (Tower). Further, we identified these assemblages within basalt and not only in sediments or hydrothermal mound deposits where work has previously been completed.

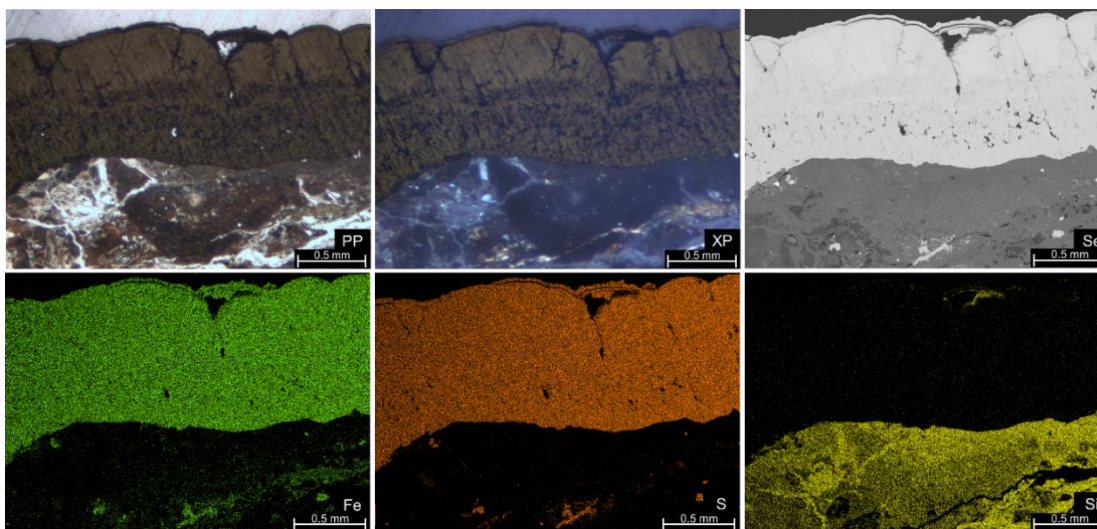


Figure 11. The petrographic micrographs and corresponding SEM/EDS elemental maps illustrate the ~mm thick pyrite encrustation on the Tower thin section (NA100-31).

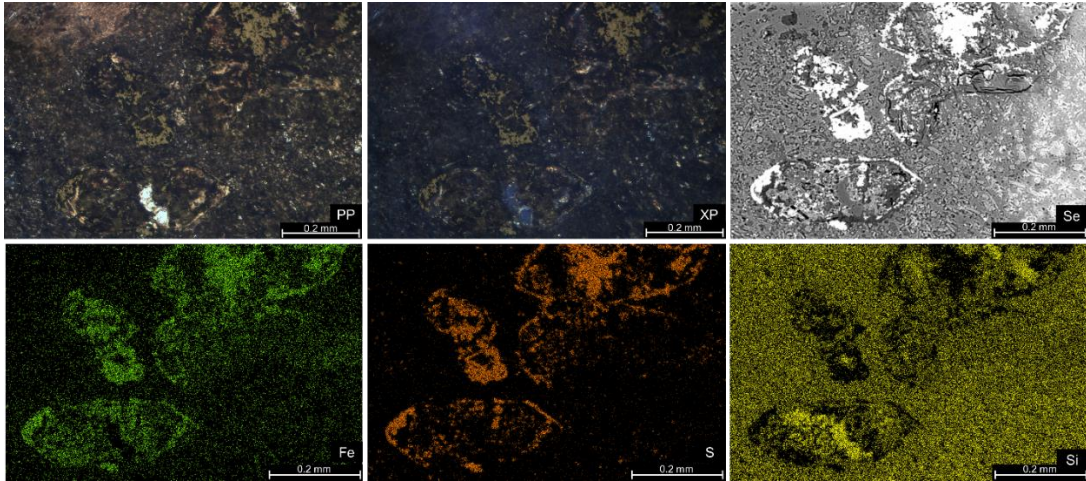


Figure 12. The petrographic micrographs and corresponding SEM/EDS elemental maps illustrate pyrite pseudomorphological replacement of euhedral olivine in the Tower region (NA100-30).

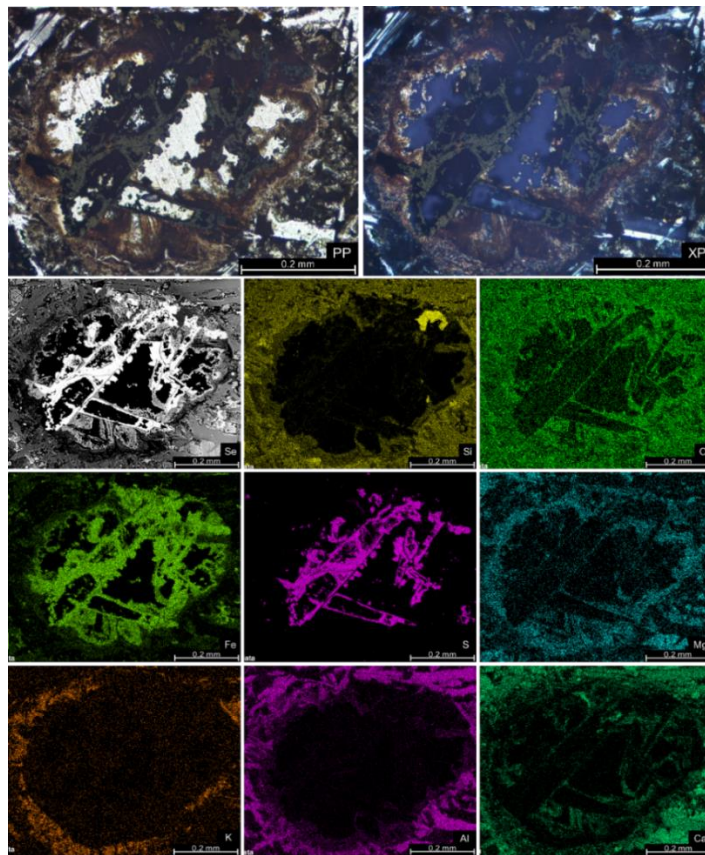


Figure 13. The petrographic micrographs and corresponding SEM/EDS elemental maps illustrate bladed pyrite within vesicle and red-orange siderite-magnesite rimming vesicle within the Tower region (NA100-30).

We tentatively identify jarosite ($\text{KFe}_3(\text{OH})_6(\text{SO}_4)_2$) in the Tower samples on the basis of EDS spectra normalized atomic wt.% abundances of mineral building elements. However, the thin section optical properties could not confirm this identification due to the spherical jarosite precipitates being smaller ($<10\mu\text{m}$) than the thickness of thin section ($30\mu\text{m}$). Jarosite always precipitated in the interiors of vesicles (Fig. 14), appearing to be among the most recent to form. There has not previously been a report of jarosite at Lō‘ihi, though other sulfates such as barite have been reported (David and Clague 1998; Davis et al., 2003).

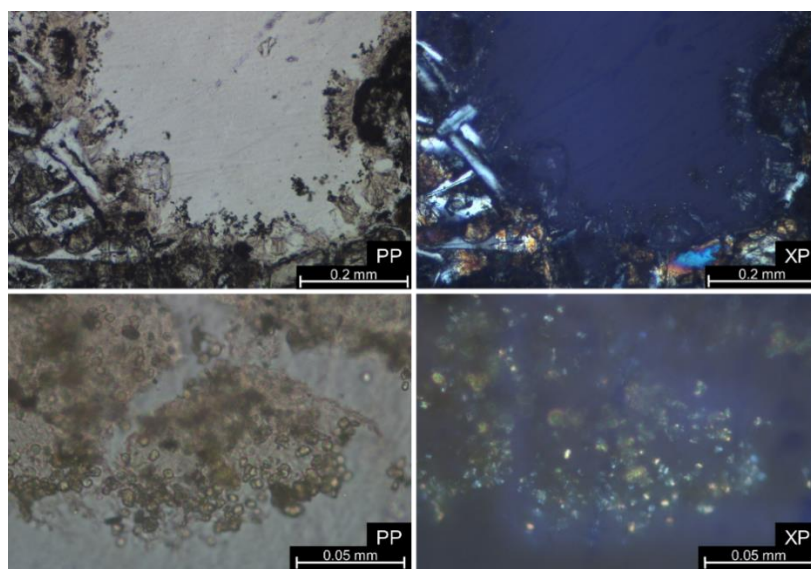


Figure 14. The petrographic micrographs illustrating $<10\mu\text{m}$ spheres of jarosite within a vesicle directly associated with amorphous impure quartz, quartz, and pyrite globules within the Tower region (NA100-31).

The Tower region samples have small clear (PP) Ti-Ba-V-O rich blade-shaped minerals (Fig. 15). These blades are within vesicles and void space and are typically associated with quartz and pyrite. This mineral has yet to be identified due to its small size. Ba mainly occurs as barite (BaSO_4); since the Ba ion is a large divalent cation, it not easily accommodated in common rock-forming minerals (Johnson et al., 2017). Barite is white to colorless and tabular, typically occurs with quartz, sulfides, clay minerals, carbonates, and iron oxides, and is among the few sulfates

previously identified at Lō‘ihi. As such it appears to be a possible identity for the blade-shaped mineral. However, it seems unlikely Ti would be a significant constituent in barite and the S signal in elemental mapping is not as strong as one would expect for a sulfate mineral.

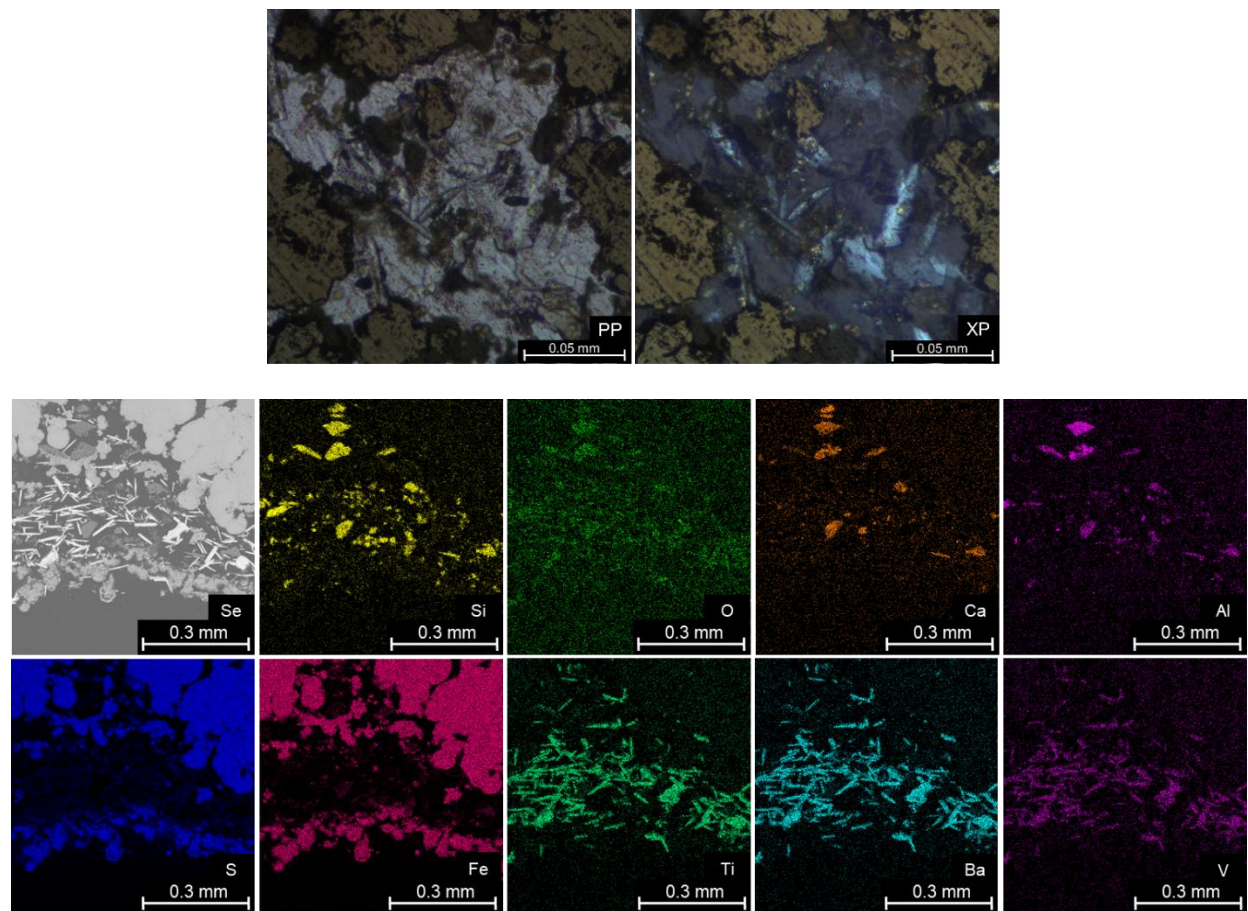


Figure 15. The top two micrographs do not correspond to the SEM/EDX maps. The petrographic micrographs illustrate the Ti-Ba-V-O blades at Tower thin section (NA100-31). The SEM/EDX image contains these blades interbedded with pyrite and minor silica.

There were three chemically distinct complex silicates identified at Tower: talc ($\text{Mg}_3\text{Si}_4\text{O}_{10}(\text{OH})_2$) to pyrophyllite ($\text{Al}_2\text{Si}_4\text{O}_{10}(\text{OH})_2$), Na-Al-rich silicate, and Mg-Fe-Al-rich silicate. These silicates appear light orangish tan to dark brown in plane polarized light, are fibrous, and infill vesicles and fractures and pseudomorphologically replace olivine. Talc-pyrophyllite forms under acidic conditions ($\text{pH} < 4$), usually $> 220^\circ\text{C}$, and in association with quartz and sulfur-bearing

deposits (D’Orazio et al., 2004). The Na-Al silicate has approximate ion ratios of 11 O, 5 Si, 2 Al, 1 Na, and minor Ca (Fig. 16b). The Mg-Fe-Al silicate has an approximate ion ratios of 10 O, 5 Si, 2 Mg, 2 Fe, 1 Al (Fig. 16c). These minerals have not yet been positively identified.

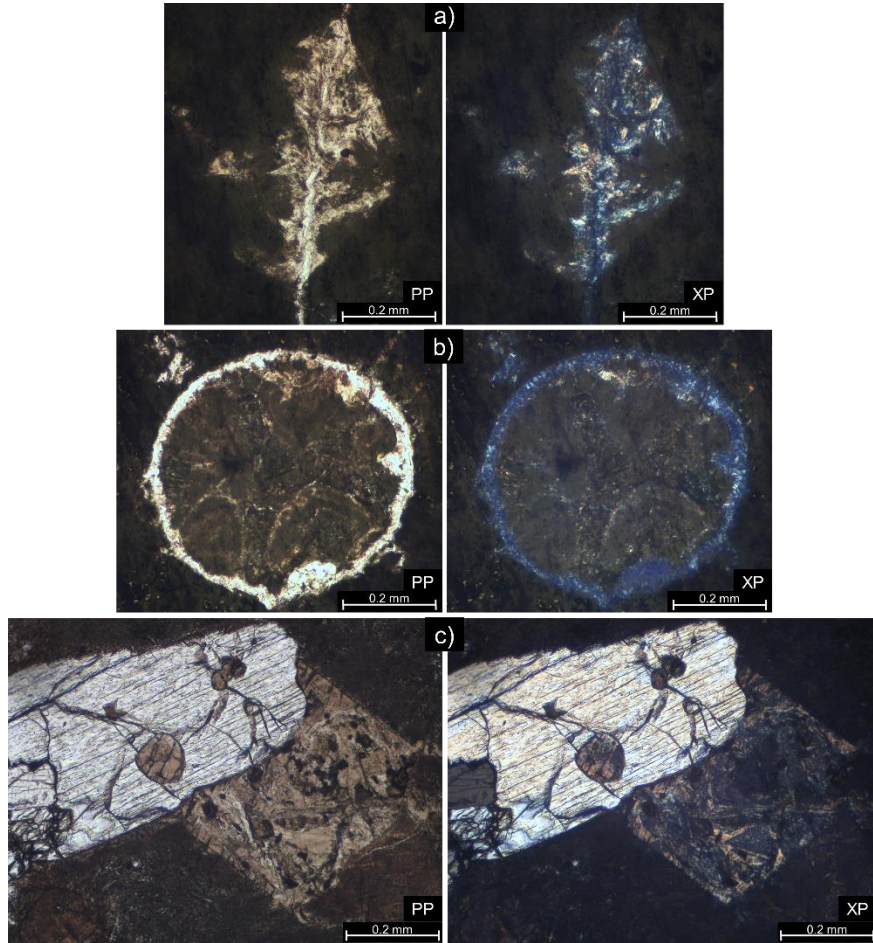


Figure 16. a) Talc to Pyrophyllite pseudomorphologically replacing olivine b) rim is Na-Al silicate within a vesicle with Mg-Fe-Al silicate in the interior c) Mg-Fe-Al silicate pseudomorphologically replacing olivine phenocryst directly associated with minimally altered pyroxene

3.2 Major and Minor Element Oxide Results

The basalts collected at hydrothermal vents were alkalic (Pohaku-a; Pohaku-b) and tholeiitic (Loihau, Tower, and Spillway) (Table 3a). Two of the ambient group samples were alkalic, five were tholeiitic, and two were transitional lava types (Table 3b), representing all three

lava compositions expected for Lō‘ihi. The total alkali ($\text{Na}_2\text{O}+\text{K}_2\text{O}$) vs silica (SiO_2) (Fig. 17) shows a progressive enrichment of silica and alkali elements in the exterior of hydrothermally-influenced basalt compared to the interior. The alkalic-tholeiitic diving line in Figure 17 is from MacDonald (1968). Major element enrichment and depletion patterns from the exterior to the interior are further evaluated in Fig. 18 using Equation 1.

Table 3a. Chemical composition of basalt samples collected in close proximity to hydrothermal vent orifices (wt.%) obtained by XRF analysis

	Pohaku M57a NA100-68		Pohaku M57b NA100-84		Loihau M2 NA100-75		Spillway M34 NA100-37		Tower M31 NA100-31 NA100-30	
	Ext.	Int.	Ext.	Int.	Ext.	Int.	Ext.	Int.	Ext.	Int.
SiO_2	48.22	48.19	48.08	48.27	47.14	46.79	48.61	47.77	51.74	48.76
TiO_2	3.43	3.38	3.41	3.4	2.18	2.06	2.52	2.41	3.36	2.58
Al_2O_3	13.71	13.66	13.68	13.7	11.22	10.68	12.65	12.11	15.38	12.67
Fe_2O_3	13.89	13.88	14.09	13.74	13.68	13.75	12.87	13.62	9.00	13.78
MgO	5.72	5.85	5.79	5.78	12.6	14.1	8.28	9.78	4.97	8.72
CaO	10.22	10.27	10.15	10.26	10.11	9.61	11.65	11.16	11.43	10.11
Na_2O	3.24	3.17	3.14	3.26	2.02	1.91	2.29	2.10	2.89	2.52
K_2O	0.83	0.87	0.89	0.86	0.45	0.48	0.53	0.45	0.58	0.29
MnO	0.18	0.18	0.18	0.18	0.18	0.18	0.18	0.18	0.15	0.17
P_2O_5	0.40	0.39	0.41	0.39	0.21	0.20	0.25	0.23	0.32	0.25
Total	99.84	99.84	99.82	99.84	99.79	99.76	99.83	99.81	99.82	99.85
LOI ^a	-0.13	0.23	-0.10	-0.04	-0.60	-0.13	1.31	1.41	2.41	3.57

^a The high loss on ignition (LOI) for Tower is linked to thermal decomposition and volatile loss (i.e., water, sulfur, carbon dioxide) from heating in a 1000°C furnace for 4 hours.

Table 3b. Chemical composition of basalt samples collected in from the ambient group, away vent orifices (wt.%) obtained by XRF analysis

	NA100-24		NA100-56		NA100-57		NA100-85		NA100-101		NA100-103		NA100-109	
	Ext.	Int.	Ext.	Int.	Ext.	Int.	Ext.	Int.	Ext.	Int.	Ext.	Int.	Ext.	Int.
SiO ₂	48.12	48.18	47.74	47.75	47.61	47.70	48.20	48.40	48.69	48.82	46.83	46.94	48.14	48.11
TiO ₂	3.38	3.36	2.44	2.43	2.40	2.43	3.42	3.43	2.40	2.43	2.07	2.07	2.68	2.68
Al ₂ O ₃	13.62	13.67	12.29	12.36	12.09	12.25	13.72	13.74	13.28	13.34	10.18	10.25	13.71	13.72
Fe ₂ O ₃	13.77	13.66	13.56	13.59	13.60	13.55	13.80	13.55	13.58	13.47	13.49	13.45	13.47	13.47
MgO	6.16	6.14	9.72	9.53	10.21	9.81	5.81	5.85	7.38	7.17	15.60	15.42	6.60	6.61
CaO	10.16	10.22	11.12	11.18	11.01	11.12	10.23	10.28	11.35	11.38	9.13	9.19	11.63	11.63
Na ₂ O	3.21	3.21	2.11	2.18	2.08	2.13	3.21	3.17	2.35	2.41	1.73	1.72	2.57	2.57
K ₂ O	0.82	0.82	0.42	0.40	0.43	0.44	0.85	0.87	0.43	0.45	0.33	0.35	0.64	0.63
MnO	0.19	0.18	0.18	0.18	0.18	0.18	0.18	0.18	0.18	0.18	0.18	0.17	0.18	0.18
P ₂ O ₅	0.39	0.39	0.23	0.23	0.23	0.23	0.40	0.40	0.24	0.24	0.19	0.19	0.27	0.27
Total	99.82	99.83	99.81	99.83	99.84	99.84	99.82	99.87	99.88	99.89	99.73	99.75	99.89	99.87
LOI	-0.25	-0.27	-0.67	-0.60	-0.71	-0.63	-0.27	-0.35	-0.70	-0.36	-0.76	-0.64	-0.30	-0.15

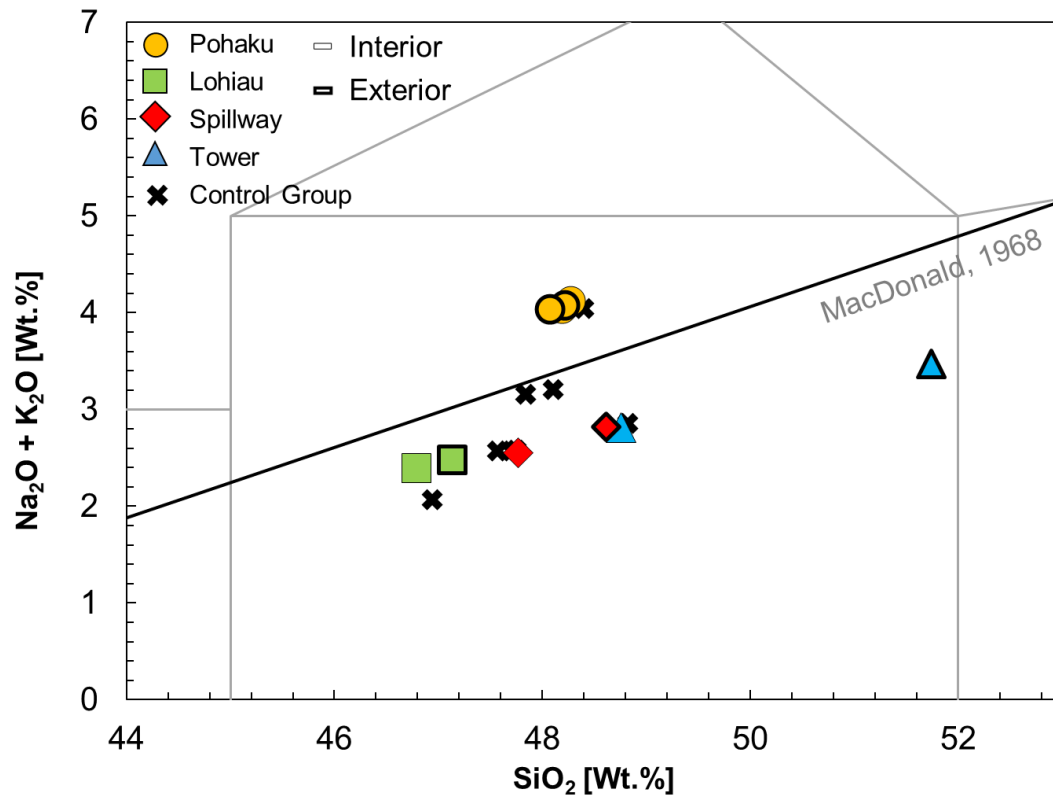


Figure 17. TAS diagram plotting the basalts collected close to hydrothermal vents (Pohaku, Lohiau, Spillway, and Tower) and the basalts collected away from known hydrothermal activity. The exterior of the hydrothermally-altered basalts have a thick outline compared to the interior. Only the interior section

of ambient-water interaction basalts are plotted in the TAS diagram due their similar values to the exterior.

The exterior to interior element oxide differences were calculated by subtracting the interior element oxide wt.% from the exterior wt.% (Fig. 18); this was done instead of a percent change because a relative abundance calculation would misleadingly amplify differences with low wt.% values even if their total wt.% change was minimal.

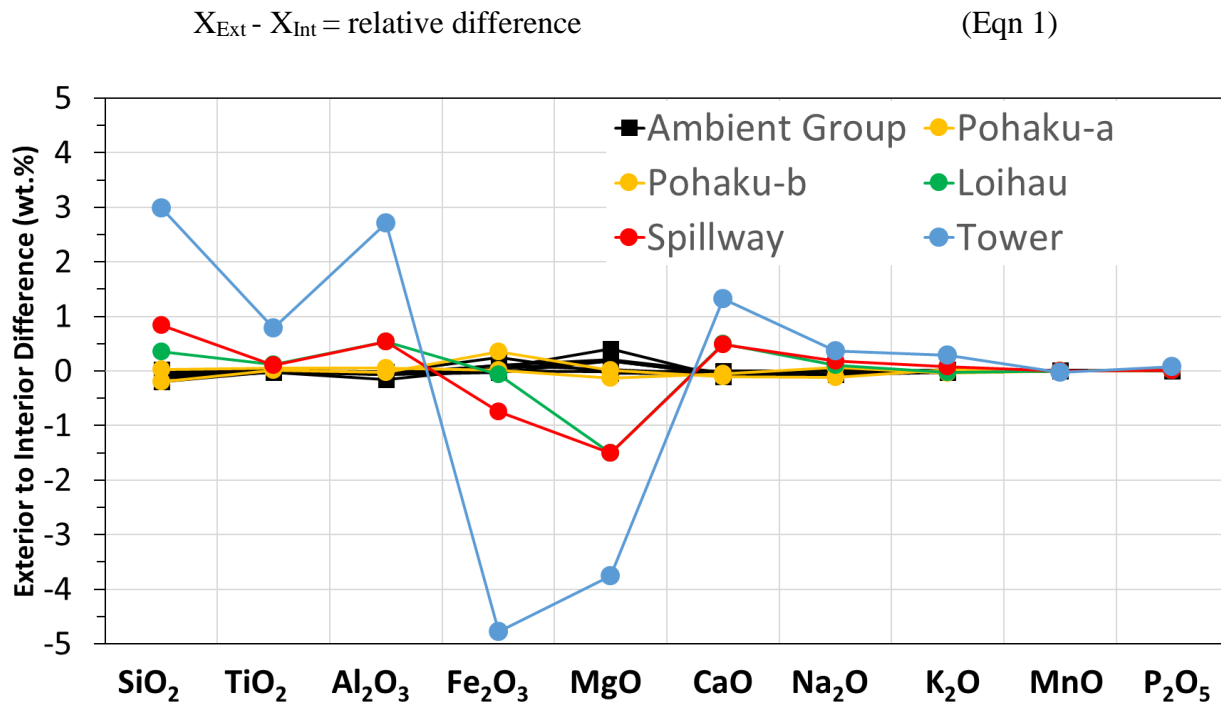


Figure 18. The element oxide exterior to interior difference in wt.%. The largest enrichments in the exterior are in Si, Al, and Ca and the largest depletions in the exterior is in Fe and Mg.

In Figure 18, there is less relative change in major elements within the ambient group and Pohaku vent sites than within the Loihau, Spillway and Tower vent sites. The greatest relative exterior enrichments at Loihau, Spillway, and Tower are in Si, Al, and Ca and the greatest depletions are in Fe and Mg. Thin section observations show that the ambient group and Pohaku vent sites were the least altered, while the Loihau, Spillway and Tower vent sites had the highest losses associated with degree of olivine breakdown. This suggests a correlation between increased

breakdown and replacement of olivine phenocrysts and microcrysts with increased bulk depletion in the exterior for Mg and Fe.

Furthermore, under normal seafloor conditions like those recorded weakly in the ambient samples, Si, Ca, Mg, Na, and K should be lost to seawater, i.e. depleted in the exterior, while Fe and Al are retained and enriched in the exterior (Kruber et al., 2008). However, the interaction with the hydrothermal seeps caused Si and Ca to become greatly enriched, Na and K to be moderately enriched, and Fe to be greatly depleted in the exterior relative to the interior (Fig. 18).

The major element oxide abundance patterns in basalts with higher degrees of alteration record a progressive divergence from typical ambient submarine basalt alteration, where insoluble Fe is depleted in the exterior instead of enriched and soluble elements Si, Ca, Na are enriched instead of depleted. The petrographic and major oxide data support a consistent pattern of increased bulk change across the samples.

3.3 Trace Element Results

XRF trace element results for the exterior and interior sections of hydrothermally- and ambient seawater-altered basalt are summarized in Tables 4a and 4b, respectively. Equation 2 was used to examine relative enrichment or depletion of an element in the exterior of a sample (Fig. 19); this showed how many times enriched or depleted a trace element was in the exterior compared to the interior of a sample.

Table 4a. Chemical composition of basalt samples collected in close proximity to hydrothermal vent orifices (ppm) obtained by XRF analysis

	Pohaku M57a NA100-68		Pohaku M57b NA100-84		Loihau M2 NA100-75		Spillway M34 NA100-37		Tower M31 NA100-31 NA100-30	
	Ext.	Int.	Ext.	Int.	Ext.	Int.	Ext.	Int.	Ext.	Int.
	F*	386	517	317	483	232	293	305	330	607
S*	2025	1241	2268	1249	1322	1108	1131	1158	12275	3111
Cl*	1556	854	1605	878	176	235	1136	400	942	146
Sc	25.7	22.7	24.6	25.8	29.4	23.3	30.8	27.8	28	27.4
V	396.8	380.4	395.7	418.5	321.9	260.9	351.7	312.5	406.3	335.8
Cr	78.8	75.6	81.3	78.4	1222.2	1279.8	813.9	730.3	95.5	528
Ni	68.5	76.2	76.1	90.8	449.1	489.3	196.6	243.5	143.3	161.9
Cu	67.8	73.7	71.4	80.7	133.3	112.8	107.6	103.3	81.4	79.1
Zn	120.6	119.7	122.1	130.2	116.2	103.1	110.1	102.9	215.5	113
Rb	15.3	14.8	15.6	16	8.1	6.9	8.6	7.4	5.7	3.3
Sr	428.4	440.8	431.7	472.3	316.4	267.2	324.4	295.4	449.5	341.5
Y	28.9	29	29.3	31.6	19.3	16.3	23.2	21.3	22.3	20.2
Zr	191	192.1	192.8	208.2	125.8	106.5	137.2	125.4	151.8	128.1
Nb	23.8	23.8	23.9	25.8	12.4	10.1	12.7	11.5	18.2	14.1
Ba	147.9	165.5	154.9	176.5	90.8	77.8	85.5	74.9	440.9	99.6
La	13.7	11.8	13.5	14.7	18.7	7.6	9.3	7.9	7.1	9.6
Ce	48.7	49.9	49.7	56.3	18.8	18.7	24.5	25.7	42.6	31.6
Nd	32.7	33.7	32.5	36.4	30.6	28.5	23	26.7	18.4	35
Ga	20.9	20.5	21.5	21.2	12.3	14.7	18.6	16.9	22.5	19
Sm	6.2	5.8	5.9	6	3.9	4.1	4.2	4.3	2.8	6.1
Pb	1.5	2.1	1.6	1.8	1	2.6	3.1	1.7	5	2.7
Th	0.8	0.9	1.1	0.2	0.09	0.09	0.09	0.6	0.6	0.09
U	0.09	0.09	0.09	0.09	0.09	0.09	0.09	0.09	0.2	0.09

*F, S, Cl values are considered an approximation with uncertainties of at least 10%.

Table 4b. Chemical composition of basalt samples collected in from the ambient group, away vent orifices (ppm)obtained by XRF analysis

	NA100-24		NA100-56		NA100-57		NA100-85		NA100-101		NA100-103		NA100-109	
	Ext.	Int.	Ext.	Int.	Ext.	Int.	Ext.	Int.	Ext.	Int.	Ext.	Int.	Ext.	Int.
F*	410	420	353	371	282	354	430	449	234	312	262	350	307	284
S*	1005	925	972	1159	1145	1117	953	1035	1514	1367	1366	1247	1984	2484
Cl*	1179	1169	128	144	121	160	1131	766	146	212	290	321	437	445
Sc	24.6	25.0	28.1	28.5	31.4	27.3	25.1	27.0	31.0	30.5	24.1	21.5	27.1	32.2
V	368.1	383.0	303.8	317.6	329.8	310.0	388.5	432.7	320.9	332.0	257.7	215.0	358.3	393.3
Cr	93.1	84.4	611.7	623.1	680.1	664.2	74.4	81.0	301.8	245.4	1586.7	1664.0	60.9	79.0
Ni	82.0	88.8	178.3	181.2	207.2	198.4	77.7	88.4	88.4	78.9	546.5	526.1	76.2	90.3
Cu	68.9	77.3	96.2	99.0	105.1	97.9	72.0	82.4	102.6	108.1	89.5	84.3	97.0	100.6
Zn	113.0	120.3	94.7	98.6	103.2	97.3	119.7	132.5	107.9	110.7	105.2	93.0	114.0	122.9
Rb	13.9	15.2	6.9	7.1	7.2	7.0	15.6	16.3	7.2	7.9	5.6	4.9	11.2	11.6
Sr	418.4	446.0	268.2	280.8	288.3	274.1	440.3	483.0	320.5	343.9	234.9	204.9	387.2	407.9
Y	27.6	29.3	19.9	20.6	21.3	20.2	29.3	32.5	21.0	22.3	17.0	15.1	22.5	23.9
Zr	182.4	193.4	116.9	121.9	125.3	119.6	193.0	213.6	131.8	139.6	104.7	92.1	143.1	152.2
Nb	22.8	23.8	10.3	11.0	11.4	10.9	24.0	26.6	12.5	13.0	9.0	8.1	16.1	17.0
Ba	146.2	157.1	59.8	65.5	64.3	66.1	153.7	174.3	79.1	83.0	53.1	45.1	127.9	124.7
La	11.7	13.4	5.8	5.6	7.5	7.2	12.9	14.9	9.8	8.8	10.6	5.0	14.2	12.8
Ce	45.9	49.4	23.2	23.4	23.3	19.6	50.3	59.2	25.3	34.1	15.0	16.5	37.2	36.5
Nd	29.8	35.8	21.9	21.9	21.5	20.3	34.3	36.3	23.4	24.5	24.7	24.4	25.9	28.5
Ga	20.1	21.1	15.9	16.4	16.4	15.6	21.3	23.0	17.0	18.6	14.4	12.8	19.8	18.8
Sm	5.8	5.7	3.6	4.5	4.3	4.1	6.4	6.3	4.8	5.6	3.8	3.7	4.7	6.2
Pb	2.1	2.9	2.1	2.3	2.4	0.5	1.8	2.1	1.8	1.7	1.1	1.9	2.4	3.4
Th	<1	1.0	1.6	0.4	0.5	0.4	0.7	<1	0.0	0.3	0.3	0.8	1.4	<1
U	<1	<1	<1	<1	<1	<1	<1	<1	0.0	<1	<1	<1	<1	<1

*F, S, Cl values are considered an approximation with uncertainties of at least 10%.

$$((X_{\text{Ext}}/X_{\text{Int}})-1)*100 = \% \text{ relative enrichment or depletion in exterior} \quad (\text{Eqn 2})$$

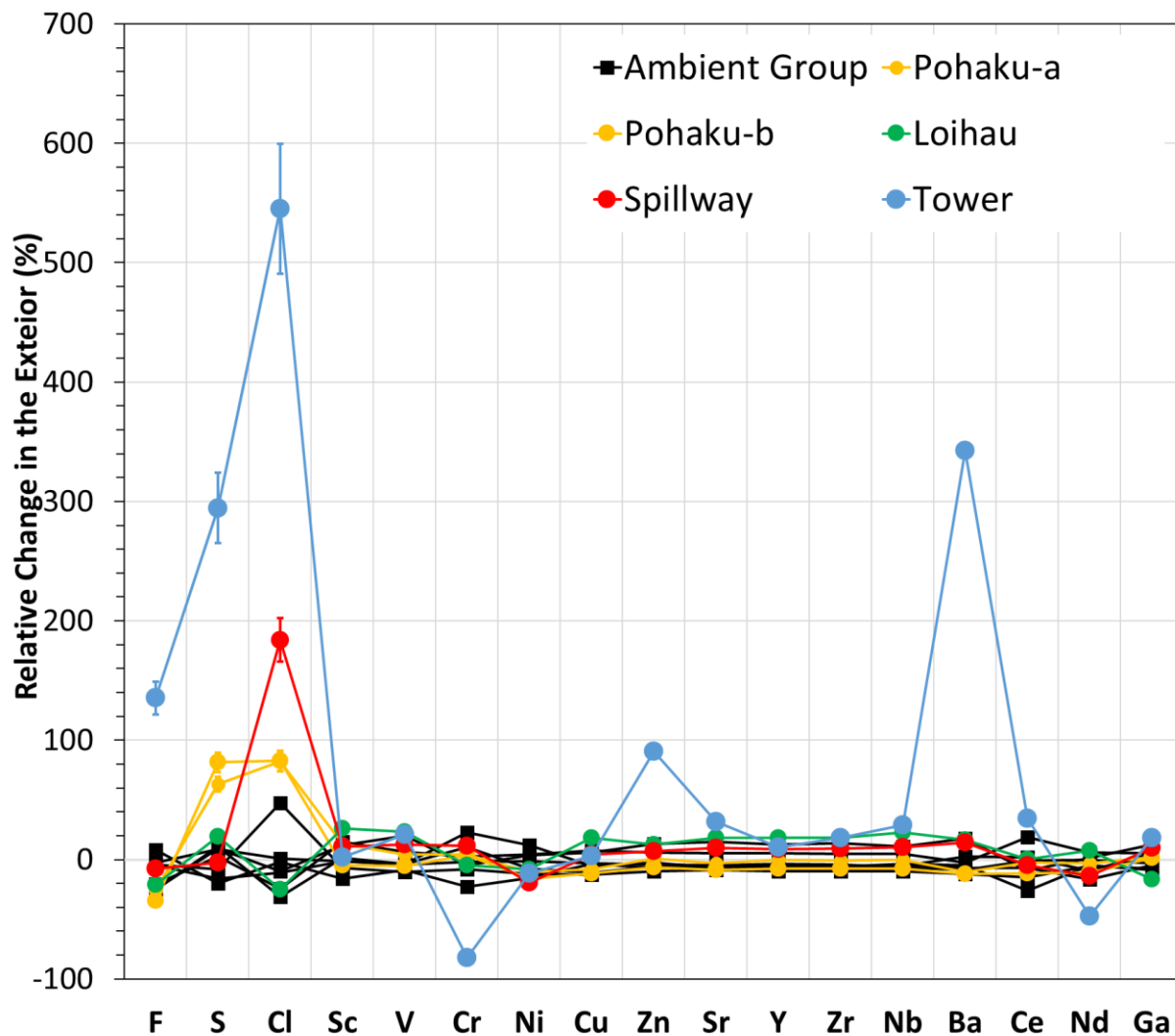


Figure 19. The trace element concentration (ppm) relative percent enrichment or depletion calculated using Equation 2. Rb, La, Sm, Pb, Th, and U were removed from this figure because of low ppm concentrations (<15ppm) causing the percent differences from exterior to interior to be exaggerated. F, S, Cl values are considered an approximation, with uncertainties of at least 10% as shown with the error bars.

In Figure 19, the Tower region stands out for having large enrichments in S, Cl, Zn, and Ba, and a large depletion in Cr. In contrast, the Loihau samples, which appeared to be the second most altered behind Tower in the petrographic and major element oxide analyses, plot within the bounds of what is observed for the ambient group.

There are large enrichments of S in the exteriors of Tower and Pohaku. The large enrichments in S are likely a reflection of sulfate and sulfide assemblages. However, these assemblages were not directly observed in the Pohaku-region thin sections, possibly due to extremely small size. Furthermore for the Tower region, a sample without the mm-thick pyrite encrustation in the exterior was powdered for XRF analysis. Even without the pyrite rind, there were large enrichments of S in the exterior of both these regions, though not at the Spillway and Loi hau hydrothermal sites. The sulfur sources in the submarine system include hydrothermally or magmatically derived gas (H_2S) and sulfate (SO_4) from seawater. The fluids at Lō'ihī are currently H_2S -poor, however the abundant S-rich mineral assemblages reflect a history with sulfur saturated hydrothermal fluids.

There are large enrichments in Cl in the exterior for Pohaku, Spillway, and Tower. There is a wide range of Cl contents reported for Lō'ihī glasses (e.g., Garcia et al., 1989); Lō'ihī has overall high Cl content relative to other Hawaiian volcanoes (Garcia et al., 1989). While the high overall Cl concentration has been proposed to originate from seawater contamination of magma (Kent et al., 1999), this does not explain the exterior relative enrichment of this element in the samples from the hydrothermal vent areas. The Cl may have been enriched in the exterior of the basalt via prolonged, warm exposure with Cl-enriched fluids, whether that Cl originated from magmatic degassing or subsurface mixing of seawater into the hydrothermal fluids. Minerals such as halite (NaCl) are also likely to precipitate but their possible preferential deposition in the exterior but could not be confirmed or denied since the washing during sample preparation would easily remove precipitated halite. The enrichments in Cl were maintained even though samples were washed prior to crushing.

The large enrichments in Ba and Zn at Tower are likely linked to sulfide and sulfate assemblages. Barite and Zn-sulfide assemblages have been previously reported at Lō‘ihi (David and Clague 1998; Davis et al., 2003). Though we did not directly observe these minerals in thin section, it is not unreasonable for them to coexist with the current assemblage. Furthermore, Lō‘ihi vent fluids are historically enriched in Ba (e.g., Karl et al., 1988) and are therefore a source for Ba enrichment.

The large depletion in Cr for the Tower region is unusual since Cr, like Zr, V, and Y does not typically appear to be affected by hydrothermal alteration (Humphris et al., 1977). There does not appear to be any enrichment/depletion in the exterior for Zr, V, and Y. Davis and Clague (1998) reported high variability in Cr concentrations of hydrothermal mound deposits. The pattern of relative depletion in the exterior is more likely to be linked to preferential precipitation of Cr-bearing mineral in the interior than preferential removal of Cr-bearing mineral in the exterior.

The Tower area basalt records the most hydrothermally influenced trace element relative abundance patterns, with element enrichments and depletions much greater than what is expected for normal seawater interaction. The secondary mineral assemblages support this varied fluid histories by the appearance of sulfide and sulfate assemblages (pyrite and jarosite) and silicates (talc-pyrophyllite). While the major element oxide petrographic data reflect consistent patterns of progressive alteration across the vent sites with Tower and Spillway having the most change followed by Loi hau and finally Pohaku, the trace element data is less clear and may be more sensitive to the time-varying hydrothermal fluid chemistries, including the impact of having had to collect the Spillway sample at a much greater distance from the vent orifice than for the other sites. Spillway therefore was expected to have greater seawater and hydrothermal fluid mixing due to the increased distance from the orifice.

Chapter 4. Discussion

Lō‘ihi has rare high temperature assemblages (e.g., sulfides and sulfates) that have been identified previously in the north rim (~Loihau) and northeast rim of Pele’s Pit following the 1996 large magmatic and tectonic event. We identified abundant pyrite and additional high temperature assemblages talc-pyrophyllite in the south east rim at Tower. We also collected basalt at the Loihau region, but did not identify any sulfide and sulfate assemblages there. This suggests steep gradients among vent sites and spatial complexity within the hydrothermal field area.

Alternately, the lack of sulfide/sulfate assemblages in the north and north east may suggest a shift in subsurface hydrothermal flow or mixing. Davis et al. (2003) returned ~2 years after the north east vent sulfide assemblage was first identified and observed dissolution and oxidation of sulfides, from which they interpreted that these minerals would not be easily or well preserved. Considering their sample collection was ~20 years prior, perhaps the large sulfide deposits from this event no longer exist and instead we are observing evidence for sulfide assemblage from a shift in the hydrothermal system where the S-rich and high temperature minerals are surfacing at a different locale and more recently.

The presence of pyrite at Tower suggests that the hydrothermal fluids percolating through the rocks during mineral deposition were reducing, S-rich, and high temperature ($>250^{\circ}\text{C}$) (David and Clague 1998). The presence of talc-pyrophyllite suggest acidic conditions ($\text{pH} < 4$) and high temperature ($>220^{\circ}\text{C}$) (D’Orazio et al., 2004). Talc-pyrophyllite is common in sulfidification deposits (D’Orazio et al., 2004). There were high temperature fluids at the Tower region in its history, which contrasts with the current S-poor, low temperature ($<100^{\circ}\text{C}$) fluids currently there and at the other hydrothermal seeps across Lō‘ihi.

In addition to the high temperature minerals identified at Tower, there are low temperature mineral assemblages at all the vent sites in Lō‘ihi (siderite, siderite-magnesite, jarosite). Carbonates are the most ubiquitous secondary minerals as they are found at every vent site. At Pohaku, Loihau, and Spillway the carbonates had siderite with partial Ca and Mg substitution for Fe in cores and siderite-magnesite rims; this compositional zoning is likely attributed to systematic changes in fluid chemistry such as dynamic levels of pCO₂ (Van Berk et al., 2010). High pCO₂ favors Fe-rich siderite, while low pCO₂ favors Mg-rich magnesite (Van Berk et al., 2010). The formation of these carbonates require elevated levels of CO₂, low temperatures <100°C, and pH <7 (Van Berk et al., 2010), all of which Lō‘ihi fluids currently satisfy. This compositional zoning of carbonates is consistent with a dynamic Lō‘ihi hydrothermal system, while also indicating regional controls since Pohaku, Loihau, and Spillway all displayed this pattern. At Tower, siderite-magnesite (low temperature assemblage) is in close association with pyrite (high temperature assemblage), therefore this area records a change in fluid supporting dynamic Lō‘ihi hydrothermalism. Carbonates were deemed the most likely phase as have been predicted at Lō‘ihi due to abundance of Fe(II) and Ca, however there had not been physically identified until this study.

Jarosite typically forms by low temperature hydrothermal alteration of pyrite, often in acidic fluids (McCubbin et al., 2009) this is consistent with the jarosite found in the interior of vesicles in thin sections with abundant pyrite. This would require vent fluids to change temperature regime over time, along with reducing hydrogen sulfide stable environments.

The geologic bulk change within basalts appears to increase Lō‘ihi hydrothermal environment for habitability in terms of nutrients (carbon and sulfur) and energetics (high redox potential elements like S). Carbon and sulfur are nutrients vital for life (CHNOPS). Within Lō‘ihi

basalts, carbon was sequestered via carbonates by bonding with Fe, Mg, and Ca and sulfur was sequestered by bonding with Fe and K (possibly also Ba and Zn). The energy budget for Lō‘ihi also has the potential to include microbial mediation of pyrite due to the presence of roughly spherical aggregates of pyrite encrustations of the Tower region samples. Although this morphology can be replicated abiotically in the lab, it has also been identified as a biotic output (Prol-Ledesma et al., 2010). Further, the alteration of olivines may be related to microbial communities, either through mediating the initial breakdown of the crystal or through chemosynthetic use of abiotically liberated Fe(II). Biologic results from teammates at Woods Hole Oceanographic Institute will assist in the determination on if pyrite-forming or olivine-destroying microbes exist at the Tower vent field.

The basalt petrographic results indicating variable alteration of olivine phenocrysts at Pohaku, Loi hau, Spillway, and Tower may be biased by preferential degradation based on olivine composition. The Pohaku region had the only alkaline lavas at the vent sites, while Loi hau, Spillway, and Tower all had tholeiitic lavas. Tholeiitic and alkaline lava types contain variable amounts of both fayalite (Fe-rich olivine) and forsterite (Mg-rich olivine) and thus it is unclear if the tholeiitic or alkali lavas would be systematically more abundant in forsterite or fayalite. Fe(II) in olivine would tend toward oxidation more than Mg at the seafloor, thus rapid degradation of Fe-rich olivine may occur over Mg-rich olivines. This potentially introduces a bias favoring fayalite-rich lava degradation over forsterite-rich lava. Since this study did not distinguish between forsterite or fayalite olivine, this potential bias cannot be more tightly constrained at this time. We would argue that the potential bias is minimal given the relative depletions in both Fe and Mg observed in the major element oxide data.

Taken as a whole, the results of this study indicate that the materials necessary for habitability occur not only in the seawater surrounding hydrothermal seeps at Lō‘ihi, but also in the rocky subsurface. We hypothesize that the elemental and molecular concentration gradients associated with the rocky substrate may even aid in inhabitation in some instances as the basalt serves to prolong the existence of the gradient compared to the diluting effects of ambient seawater; such areas may be very spatially discontinuous, however, depending on the fluid history. Thus, future work on Enceladus should, if possible, consider not only the habitability of the water but also the warm, nutrient-enriched rocky seafloor. Further work from our microbiology and geochemistry collaborators should indicate which elements or molecules should be enriched in Enceladus’ seawater if the seafloor is, indeed, inhabited, and may provide useful guides for continued examination of the icy shell and water geysers, which are far more accessible for study than direct examination of the seafloor.

The geologic history of Enceladus is largely unknown. Therefore, it is within reasonable bounds that Enceladus has effectively already altered well beyond what we would consider basalt due to billions of years of water-rock alteration. In that case, the processes we are exploring may offer a glimpse into much earlier in Enceladus’s history instead of modern day.

Chapter 5. Conclusion

The submarine basaltic rocks collected from the Lō‘ihi vent orifices record a spatially and temporally complex hydrothermal system. These changes occur on a local scale within a vent orifice and on a regional scale among multiple vent orifices across the edifice. On a local level, the Tower vent basalt has both high (pyrite, talc-pyrophyllite) and low temperature assemblages (jarosite, siderite-magnesite) therefore providing an example of a temporally variable system consistent with past observations of fluid temperatures. The Tower area is also spatially complex with preferential enrichments of Si-rich precipitates in the exterior and Fe-rich precipitates in the interior. Furthermore, carbonates found at Pohaku, Loihau, and Spillway all show a similar pattern of compositional zoning (siderite-magnesite rim and siderite core) suggesting regional variability in the source of CO₂ at Lō‘ihi. Additionally there are sulfide and sulfate assemblages reported in 1998 in the north and northeast hydrothermal vent fields, while in 2018 sulfide and sulfate assemblages were only identified in the south east, possibly suggesting a shifting subsurface source. The trace element data show different enrichment and depletion patterns in the exterior, with Tower showing the largest change from exterior to interior in Cl, S, Zn, Ba, and Cr; this supports varying fluid histories that influenced the vent basalts.

The basalt petrographic and geochemical results provide evidence for variable alteration at Pohaku, Loihau, Spillway, and Tower, ordered least to most alteration. The variety of alteration states could reflect the duration that the basalt was in direct contact with hydrothermal fluids and/or the ion content of the hydrothermal fluids and/or rock type. The behaviors of major elements Si, Ca, Fe and Al at Loihau, Spillway and Tower differ in behavior and magnitude from the basalt that was only affected by ambient seawater. The major element oxide pattern behavior would suggest that the aqueous environment at the vents enabled net loss of Fe and Mg but retention of

Si, Ca, Al in the exterior over the interior. The behavior of Fe, Si, and Ca contrasts with typical submarine basalt alteration due to a change from ion undersaturated and oxidizing (seawater conditions) to ion saturated and reducing (hydrothermal conditions). Both the petrographic and major oxide investigation shows a consistent pattern in increased bulk change correlated to the increased degree of olivine phenocryst alteration where there are progressively greater wt.% differences from the exterior to interior within each sample as the degree of alteration progresses.

These results give rise to the temporal persistence of the S-rich hydrothermal influx within the aqueous environment and the spatial complexity and steepness of gradients of Lō'ihī hydrothermal system. Future work should examine these differences at a local scale with replicates across a vent site and drills that enable sampling into the outcrop. Geologic results provide insight to the element mobility behavior within basalts under Lō'ihī hydrothermal and seawater mixing at the subsurface as well as provide insight into the past history of these vents. These results will be incorporated into geochemical models to expand the range of Earth-based hydrothermal vents to be related later to Enceladus habitability potential.

Chapter 6. Closing Statement

The SUBSEA team visited Lō‘ihi in 2018 as an analog to study volcanically-hosted water-rock hydrothermal reactions suggested to occur at Saturn’s moon, Enceladus. This research is motivated by increasing the understanding of the microbial habitability potential of Enceladus. The SUBSEA science team includes geology, geochemistry, and microbiology. The geologic findings from basalt collected across the hydrothermal field will be combined with the aqueous geochemistry and microbiology results and incorporated into a cumulative geochemical model for Lō‘ihi that will be subsequently adjusted to be more applicable to Enceladus as additional data becomes available. Including Lō‘ihi, which is a low temperature and pressure intraplate system, will make the nutrient and energy budget model for Enceladus more robust. This thesis better constrains the extent that hydrothermal fluids at the seafloor of Lō‘ihi influence submarine mafic rock alteration processes to assist in this model. Elements that are enriched in the exterior are readily available at the water-rock interface for microbes to use as energy sources and in many cases these enrichments differ from typical submarine basalt alteration. This work has identified major chemical components of the secondary mineral assemblages at each vent site which provide insight into the fluid history at Lō‘ihi allowing for more accurate time series geochemical models. This study helps understand the spatial complexity that exists at volcanically hosted hydrothermal vent sites within Ocean Worlds in our Solar System.

References

- Amend, J., McCollom, T., Hentscher, M., & Bach, W. (2011). Catabolic and anabolic energy for chemolithoautotrophs in deep-sea hydrothermal systems hosted in different rock types. *Geochimica et Cosmochimica Acta*, 75(19), 5736-5748.
- Baker, E., & German, C. (2004). On the global distribution of hydrothermal vent-fields. *Mid-Ocean Ridges: Hydrothermal Interactions Between the Lithosphere and Oceans*, *Geophys. Monogr. Ser.*, 148, 245-266.
- Baker, E., Chen, Y., & Phipps Morgan, J. (1996). The relationship between near-axis hydrothermal cooling and the spreading rate of mid-ocean ridges. *Earth and Planetary Science Letters*, 142(1-2), 137-145.
- Burgin, A., Yang, W., Hamilton, S., & Silver, W. (2011). Beyond carbon and nitrogen: How the microbial energy economy couples elemental cycles in diverse ecosystems. *Frontiers in Ecology and the Environment*, 9(1), 44-52.
- Byers, C., Garcia, M., Muenow, D. (1985). Volatiles in pillow rim glasses from Loihi and Kilauea volcanoes, Hawaii. *Geochimica et Cosmochimica Acta*, 49(9), 1887-1896.
- Caplan-Auerbach, J., & Duennebier, F. (2001). Seismic and acoustic signals detected at Loihi Seamount by the Hawai'i Undersea Geo-Observatory, *Geochemistry, Geophysics, Geosystems*, 2(5).
- Clague, D., McClain, J., & Zierenberg, R. (2019). Lava flows erupted in 1996 on North Gorda Ridge Segment and the Geology of the nearby Sea Cliff hydrothermal vent field from 1-m Resolution AUV Mapping. *in prep.*
- Davis, A., & David, C. (1998). Changes in the hydrothermal system at Loihi Seamount after the formation of Pele's pit in 1996. *Geology*, 26(5), 399-402.

- Davis, A., Clague, D., Zierenberg, R., Wheat, C., & Cousens, B. (2003). Sulfide formation related to changes in the hydrothermal system on Loihi seamount, Hawai'i, following the seismic event in 1996. *The Canadian Mineralogist*, *41*, 457-472.
- D'Orazio, M., Boschi, C., & Brunelli, D. (2004). Talc-rich hydrothermal rocks from the St. Paul and Conrad fracture zones in the Atlantic Ocean. *European Journal of Mineralogy*, *16*(1), 73-83.
- Duennebier, F., Becker, N. C., Caplan-Auerbach, J., Clague, D. A., Cowen, J., Cremer, M., ... & Midson, B. P. (1997). Researchers rapidly respond to submarine activity at Loihi Volcano, Hawaii. *Eos*, *78*(22), 229.
- Escoube, R., Rouxel, O., Edwards, K., Glazer, B., & Donard, O. (2015). Coupled Ge/Si and Ge isotope ratios as geochemical tracers of seafloor hydrothermal systems: Case studies at Loihi Seamount and East Pacific Rise 9°50'N. *Geochimica et Cosmochimica Acta*, *167*, 93-112.
- Farmer, J. (2018). Habitability as a Tool in Astrobiological Exploration. In J. Farmer, *From Habitability to Life on Mars* (pp. 1-12). Elsevier.
- Fisher, R. V., & Schmincke, H. U. (1984). Submarine volcanoclastic rocks. In *Pyroclastic Rocks* (pp. 265-296). Springer, Berlin, Heidelberg.
- Francis, P., Oppenheimer, C., & Stevenson, D. (1993). Endogenous growth of persistently active volcanoes. *Letters to Nature*, *366*(6455), 554-557.
- Furnes, H., Staudigel, H., Thorseth, I., Torsvik, T., Muehlenbachs, K., Tumyr, O., . . . Tumyr, O. (2001). Bioalteration of basaltic glass in the oceanic crust. *Geochem. Geophys. Geosyst*, *2*, 268.

- Garcia, M., Caplan-Auerbach, J., De Carlo, E., Kurz, M., & Becker, N. (2006). Geology, geochemistry and earthquake history of Lōihi Seamount, Hawaii's youngest volcano. *Chemie der Erde - Geochemistry*, 66(2), 81-108.
- Garcia, M., Foss, D., West, H., & Mahoney, J. (1995). Geochemical and isotopic evolution of Loihi Volcano, Hawaii. *Journal of Petrology*, 36(6), 1647-1674.
- Garcia, M., Jorgenson, B., Mahoney, J., Ito, E., Irving A. (1993). An evaluation of temporal geochemical evolution of Loihi summit lavas: results from Alvin submersible dives. *Journal of Geophysical Research*, 98(B1), 537-550.
- Garcia, M., Muenow, D., Aggrey, K., & O'Neil, J. (1989). Major element, volatile, and stable isotope geochemistry of Hawaiian submarine tholeiitic glasses. *Journal of Geophysical Research*, 94(B8).
- Glazer, B., & Rouxel, O. (2009). Redox speciation and distribution within diverse Iron-dominated microbial habitats at Loihi Seamount. *Geomicrobiology Journal*, 26(8), 606-622.
- Glein, C., Postberg, F., & Vance, V. (2018). The Geochemistry of Enceladus: Composition and Controls. In C. Glein, F. Postberg, & V. Vance, *Enceladus and the Icy Moons of Saturn* (pp. 39-56). University of Arizona Press.
- Guillou, H., Garcia, M., & Turpin, L. (1997). Unspiked K-Ar dating of young volcanic rocks from Loihi and Pitcairn hot spot seamounts. *Journal of Volcanology and Geothermal Research*, 78(3), 239-249.
- Hedrich, S., Schlömann, M., & Barrie Johnson, D. (2011). The iron-oxidizing proteobacteria. *Microbiology*, 157(6), 1551-1564.
- Hilton, D., McMurty, G., & Goff, F. (1998). Large variations in vent fluid CO₂/He ratios signal rapid changes in magma chemistry at Loihi seamount, Hawaii. *Nature*, 396(6709), 359.

- Hsu, H., Postberg, F., Sekine, Y., Shibuya, T., Kempf, S., Hornyi, M., . . . Srama, R. (2015). Ongoing hydrothermal activities within Enceladus. *Nature*, 519(7542), 207.
- Humphris, S., & Thompson, G. (1978). Trace element mobility during hydrothermal alteration of oceanic basalts. *Geochimica et Cosmochimica Acta*, 42(1), 127-136.
- Iess, L., Stevenson, D., Parisi, M., Hemingway, D., Jacobson, R., Lunine, J., . . . Tortora, P. (2014). The gravity field and interior structure of Enceladus. *Science*, 344(6179), 78-80.
- Karl, D., McMurtry, G., Malahoff, a., & Garcia, M. (1988). Loihi Seamount, Hawaii: a mid-plate volcano with a distinctive hydrothermal system. *Nature*, 335(6190), 532.
- Kent, A., Clague, D., Honda, M., Stolper, E., Hutcheon, I., & Norman, M. (1999). Widespread assimilation of a seawater-derived component at Loihi Seamount, Hawaii. *Geochimica et Cosmochimica Acta*, 63(18), 2749-2761.
- Konn, C., Charlou, J., Holm, N., Mousis, O. (2015). The production of methane, hydrogen, and organic compounds in ultramafic-hosted hydrothermal vents of the mid-atlantic ridge. *Astrobiology*, 15(5), 381-399.
- Lineweaver, C., & Chopra, A. (2012). The Habitability of Our Earth and Other Earths: Astrophysical, Geochemical, Geophysical, and Biological Limits on Planet Habitability. *Annual Review of Earth and Planetary Sciences*, 40(1), 597-623.
- Lowenstern, J. (2001). Carbon dioxide in magmas and implications for hydrothermal systems. *Mineralium Deposita*, 36(6), 450-502.
- Malahoff, A., McMurtry, G., Wiltshire, J., & Yeh, H. (1982). Geology and chemistry of hydrothermal deposits from active submarine volcano Loihi, Hawaii. *Nature*, 298(5871), 234.

- McCubbin, F., Tosca, N., Smirnov, A., Nekvasil, H., Steele, A., Fries, M., & Lindsley, D. (2009). Hydrothermal jarosite and hematite in a pyroxene-hosted melt inclusion in martian meteorite Miller Range (MIL) 03346: Implications for magmatic-hydrothermal fluids on Mars. *Geochimica et Cosmochimica Acta*, 73(16), 4907-4917.
- McKay, C., Anbar, A., Porco, C., & Tsou, P. (2014). Follow the Plume: The Habitability of Enceladus. *Astrobiology*, 14(4), 352-355.
- Plas, L., & Tobi, A. (1965). A chart for judging the reliability of point counting results. *American Journal of Science*, 263(1), 87-90.
- Porco, C. (2006). Cassini Observes the Active South Pole of Enceladus. *Science*, 311(5766), 1393-1401.
- Postberg, F., Kempf, S., Schmidt, J., Brilliantov, N., Beinsen, A., Abel, B., . . . Srama, R. (2009). Sodium salts in E-ring ice grains from an ocean below the surface of Enceladus. *Nature*, 459(7250), 1098-1101.
- Postberg, F., Schmidt, J., Hillier, J., Kempf, S., & Srama, R. (2011). A salt-water reservoir as the source of a compositionally stratified plume on Enceladus. *Nature*, 474(7353), 620.
- Prol-Ledesma, R., Canet, C., Villanueva-Estrada, R., & Ortega-Osorio, A. (2010). Morphology of pyrite in particulate matter from shallow submarine hydrothermal vents. *American Mineralogist*, 95(10), 1500-1507.
- Rouxel, O., Toner, B., Germain, Y., & Glazer, B. (2018). Geochemical and iron isotopic insights into hydrothermal iron oxyhydroxide deposit formation at Loihi Seamount. *Geochimica et Cosmochimica Acta*, 220, 449-482.

- Sakai, H., Nakai, T., Ishibashi, J., Gamo, T., Fujioka, K., Watanabe, M., . . . Tilbrook, B. (1987). Hydrothermal Activity On The Summit Of Loihi Seamount, Hawaii. *Geochemical Journal*, 21(1), 11-21.
- Schipper, C. I., & White, J. D. (2010). No depth limit to hydrovolcanic limu o Pele: analysis of limu from Lōihi Seamount, Hawaii. *Bulletin of volcanology*, 72(2), 149-164.
- Schubert, G., Anderson, J., Travis, B., Palguta, J. (2007). Enceladus: Present internal structure and differentiation by early and long-term radiogenic heating. *Icarus*, 118(2), 345-355.
- Sedwick, P., McMurtry, G., & Macdougall, J. (1992). Chemistry of hydrothermal solutions from Pele's vents, Loihi Seamount, Hawaii. *Geochimica et Cosmochimica Acta*, 56(10), 3643-3667.
- Seewald, J. (2017). Detecting molecular hydrogen on Enceladus. *Science*, 356(6334), 132-133.
- Sekine, Y., Shibuya, T., Postberg, F., Hsu, H., Suzuki, K., Masaki, Y., . . . Sirono, S. (2015). High-temperature water-rock interactions and hydrothermal environments in the chondrite-like core of Enceladus. *Nature Communications*, 6, 8604.
- Spencer, J., & Nimmo, F. (2013). Enceladus: An Active Ice World in the Saturn System. *Annual Review of Earth and Planetary Sciences*, 41, 693-717.
- Spencer, J., Pearl, J., Segura, M., Flasar, F., Mamoutkine, A., Romani, P., . . . Lopes, R. (2006). Cassini encounters Enceladus: Background and the discovery of a south polar hot spot. *Science*, 311(5766), 1401-1405.
- Toner, B., Berquó, T., Michel, F., Sorensen, J., Templeton, A., & Edwards, K. (2012). Mineralogy of iron microbial mats from Loihi Seamount. *Frontiers in Microbiology*, 3, 118.

- Van Berk, W., Ilger, J., Fu, Y., & Hansen, C. (2011). Decreasing CO₂ partial pressure triggered Mg-Fe-Ca carbonate formation in ancient Martian crust preserved in the ALH84001 Meteorite. *Geofluids*, 11(1), 6-17.
- Waite, J., Glein, C., Perryman, R., Teolis, B., Magee, B., Miller, G., . . . Bolton, S. (2017). Cassini finds molecular hydrogen in the Enceladus plume: Evidence for hydrothermal processes. *Science*, 356(6334), 155-159.
- Wheat, G., Jannasch, H., Plant, J., Moyer, C., Sansone, F., & McMurtry, G. (2000). Continuous sampling of hydrothermal fluids from Loihi Seamount after the 1996 event. *Journal of Geophysical Research*, 105(B8), 19353-19367.
- Zolotov, M. (2007). An oceanic composition on early and today's Enceladus. *Geophysical Research Letters*, 34(23).